Design of a Robust Controller for DC/DC Converter-Electrolyzer Systems Supplied by μWECSs subject to Highly Fluctuating Wind Speed

Francesco Alonge[a], Stefania Maria Collura[a], Filippo D'Ippolito[a,*], Damien Guilbert[b], Massimiliano Luna[c], Gianpaolo Vitale[d]

[a] Università degli Studi di Palermo, Dipartimento di Ingegneria (DI), Viale delle Scienze ed.10, 90128 Palermo, Italy

[b] Université de Lorraine, IUT de Longwy, Group of Research in Electrical Engineering of Nancy (GREEN), 186 rue de Lorraine, 54400 Cosnes-et-Romain, France

[c] CNR-INM, National Research Council of Italy, Institute of Marine Engineering, Palermo, Italy

[d] CNR-ICAR, National Research Council of Italy, Institute for High Performance Computing and Networking, Palermo, Italy

[*]corresponding author. Phone: +3909123863606

e-mail: filippo.dippolito@unipa.it

Abstract

A buck-based, isolated, high-voltage-ratio DC/DC converter that allows supplying a proton exchange membrane (PEM) electrolyzer from a micro-wind energy conversion system (μWECS) has been recently presented. It exhibits low ripple at the switching frequency on the output voltage and current and represents an attractive solution for low-cost hydrogen production. In this paper, a more accurate mathematical model of such a converter is derived and discussed. Then, a model-based robust controller is designed in the frequency domain using the Internal Model Control structure and in the context of H_2/H_∞ optimal control. The controller satisfies the condition of robust stability and behavior, i.e., it guarantees stability and the desired behavior in the presence of parametric variations and unmodelled dynamics. In particular, the robustness in the presence of variations of DC-link voltage and buck input inductance is verified from the theoretical point of view. The validation of the controller is performed by integrating it into a detailed switching model of the DC/DC converter, which is implemented on a widely used circuit-oriented simulator. Good results are obtained in terms of dynamic and steady-state behavior, even in the presence of the above variations. A comparison is also carried out with the results obtained using an integral controller designed on the basis of the above mathematical model. Such a comparison shows the superiority of the robust controller over the integral controller in all the operating conditions, especially when the DC-link voltage is subject to significant variations and is affected by a non-negligible low-frequency ripple due to the presence of the diode rectifier at the output of the μWECS.

Keywords

Electrolyzer, stand-alone wind generator, buck converter, full-bridge converter, model-based control techniques, robust control.

NOMENCLATURE

d	duty cycle
E_{el}	reversible voltage of the electrolyzer (V)
i_B	input current of full bridge converter (A)
i_{el}	input current of the electrolyzer (A)
i_{it}	transformer input current (A)
i_{ot}	transformer output current (A)

$N = v_{it}/v_{ot}$	turns ratio of the transformer
R_{el}	resistance of the electrolyzer (Ω)
v_B	input voltage of full bridge converter (V)
v_D	output voltage of the diode bridge (V)
V_{dc}	voltage of the DC bus (V)
v_{el}	input voltage of the electrolyzer (V)
v_i	voltage on the diode of the buck converter (V)
v_{it}	transformer input voltage (V)
v_{ot}	transformer output voltage (V)

1. INTRODUCTION

Hydrogen is a clean and efficient energy carrier; as such, it is considered as a promising solution for a sustainable future. As a matter of fact, hydrogen can be used as a storage system with a very high energy density (120 MJ/kg); furthermore, it can be employed in fuel cells to generate electricity or combined heat and power, producing water as the only waste product [1]. The use of electrolyzers supplied from renewable energy sources is a promising solution to minimize the environmental impact significantly [2]. In particular, the possibility of supplying electrolyzers with wind energy has been studied not only for grid-connected plants [3-6] but also in stand-alone configurations [7-9]. As for this second scenario, the combination of a micro-wind energy conversion system (μWECS), involving power levels under 10 kW, and a proton exchange membrane (PEM) electrolyzer is very attractive for its low cost and easy installation. However, the use of a suitable DC/DC converter is crucial to interface the μWECS with the electrolyzer.

The current state of the art of DC/DC converter topologies for electrolyzer applications was presented in [10], where different converter topologies were compared in terms of output current ripple at the switching frequency, conversion ratio, energy efficiency, and power switch fault-tolerance. In [11], a theoretical and experimental comparative analysis of DC/DC converters was carried out considering full-bridge converters supplying the load through an LC filter, with or without a transformer. It was proved that DC/DC converters encompassing transformers present better performance for supplying electrolyzers from wind generators. The same isolated converter topology was also studied in [12] performing both simulations in PSIM (Powersim) software environment and experimental tests. In [13], a comparative analysis among three topologies of isolated converters for supplying electrolyzers from renewable generators was performed, and the topology allowing zero-voltage switching in the whole range of operation, thus reducing switching losses, was found. In [14], an interesting buck-based, isolated, DC/DC converter topology for interfacing a

μWECS with an electrolyzer was presented. Such a topology allows obtaining high voltage ratio, high efficiency, and low output current ripple at the switching frequency. The mathematical model of the converter was obtained assuming some simplifying hypotheses. Then, a classical integral-type controller was designed for constructing a control loop of the input current of the electrolyzer, and the operation of the whole system was validated in a single scenario, exhibiting a satisfying behavior.

As a matter of fact, power electronic converters supplying electrolyzers from μWECSs are not easy to control, especially in the presence of highly fluctuating wind speed and when the mechanical inertia of the wind generator is low. The most frequently used approach to cope with energy flow control in micro-grids encompassing sensitive devices such as fuel cells and electrolyzers is resorting to fuzzy logic techniques. For example, a fuzzy logic-based PID controller is designed in [15] for controlling hydrogen production for a fuel cell inserted in a stand-alone microgrid, aiming at reducing energy fluctuations. The controller is tuned using Artificial Bee Colony (ABC) optimization algorithm, described in [16], which allows defining scale factors, membership functions, and fuzzy rules simultaneously. Both the electrolyzer and the fuel cell are modeled in terms of the active/reactive powers needed for their operations. In [17], fuzzy control methodology is also applied to a stand-alone wind energy-based conversion scheme for controlling the output of the PWM inverter.

In [18] a micro-grid is investigated which encompasses a wind generator as the primary source of energy and a micro-gas turbine for supplying a housing load and an electrolyzer, whose hydrogen tank supplies a fuel cell in turn. The fuel cell and the electrolyzer are modeled by means of first-order transfer functions, i.e., with a gain and a real pole. Both transfer functions have the grid frequency variation as input, whereas the outputs are the load power variation in the electrolyzer and the fuel cell, respectively. The DC/DC converter that should supply the electrolyzer is not considered. The paper focuses on the stability of micro-grid operation and discusses the control techniques for combining a micro-turbine with the fuel cell-electrolyzer hybrid system to expand the microgrid's ability to solve power quality issues resulting from frequency fluctuations.

In [19] a photovoltaic field is assumed to supply a micro-grid encompassing AC loads and a DC/DC converter-electrolyzer system that produces and stores hydrogen to supply a fuel cell. The focus of the paper

is to model the various components of the micro-grid to expand the library of the simulation platform Transient System Simulation Tool (TRNSYS), which is a flexible simulation program that allows the user to integrate self-developed models. The discussed control strategies aim at the individuation of the best sequence of use of the various energy sources in a year. These strategies seem to be heuristic.

In [20], a power system stabilizer (PSS) equipped with a diesel generator is proposed for reducing frequency fluctuations in the same microgrid studied in [15]. Both the electrolyzer and the PSS are controlled using robust PID controllers, whose parameters are tuned using ABC evolutionary optimization techniques, according to mixed H_2/H_∞ control methods. However, evolutionary algorithms often produce suboptimal results; hence, the returned set of controller parameters is not always the optimal one. Furthermore, proving the stability and robustness of fuzzy logic controllers is not always easy or possible at all.

For these reasons, in this paper, a model-based robust controller is designed for a DC/DC converter that supplies an electrolyzer from a wind generator. As a matter of fact, robust controllers have been used to control high-power (above hundreds of kilowatts), grid-connected wind turbines performing vector control of current, flux, and speed of the associated electrical generator [21]-[23]. The control method illustrated in the present paper is based on the same theoretical background as in [21]-[23] and [29]; however, considering that the DC/DC converter is described by means of a SISO model, the control method is developed according to the procedure described in chapters 1-5 of [26].

The DC/DC converter considered in the paper is the one presented in [14]. A more accurate model of such a converter is obtained assuming the transformer as ideal but considering an equivalent turn ratio. In this way, a Linear Time-Invariant (LTI) model is obtained, which is able to reproduce the steady-state behavior in a satisfying manner. Based on this model, a robust controller is designed using H_2/H_∞ optimal control techniques. Unlike paper [20], the H_2/H_∞ approach is applied to the model in the frequency domain using the Internal Model Control (IMC) structure, rather than in the context of evolutionary optimization. The robust control approach allows considering the high-frequency dynamics of the system as unmodelled dynamics, thus simplifying the structure of the controller. Furthermore, such a control maintains the stability and the desired behavior in the presence of both the unmodelled dynamics and large wind speed fluctuations. This happens because these dynamics do not influence the structure of the controller directly; rather, they

influence the values of some of the controller parameters. The analysis of the robustness against variations of the DC-link voltage supplying the converter and buck input inductance is carried out from a theoretical point of view. Then, the validation of the controller is performed by integrating it into a detailed switching model of the DC/DC converter that is implemented on a circuit-oriented simulator, i.e., the Simulation Platform for Power Electronic Systems (PLECS). This simulator accurately reproduces the real behavior of the DC/DC converter, and it is widely used in the industrial environment.

The paper is organized as follows. In Section 2, the physical system under study is described in detail, and the accurate mathematical model is devised. Section 3 highlights the limits of the classic controller, presents the design of the robust controller, and evaluates its robustness against variations of input voltage and buck input inductance. The validation of the controller in the PLECS environment is presented in Section 4. Finally, Section 5 draws the conclusions.

2. PHYSICAL SYSTEM AND MATHEMATICAL MODEL

2.1 Physical system

The considered high-voltage-ratio DC/DC converter interfacing a μWECS with a PEM electrolyzer was designed in [14]. Its electric scheme is shown in Fig. 1, and it will be described in the following. In a μWECS, the output of the Permanent Magnet Synchronous Generator (PMSG) coupled to the wind turbine is typically connected to a three-phase diode rectifier and a bulk capacitor. This configuration implies that the electrical machine inside a μWECS is not actively controlled, and the whole set {turbine, generator, rectifier, bulk capacitor} can be regarded as a variable DC voltage generator V_{dc}. In the case under study, the nominal DC voltage is $V_{dc,rated} = 200$ V, and $V_{dc} \in [150, 220]\, V$ depending on the operating conditions. This voltage is applied to a Buck DC/DC Converter (BC) working in Continuous Conduction Mode (CCM) for a preliminary voltage reduction. The output voltage of the BC (i.e., about 80 V when $V_{dc} = V_{dc,rated}$) is applied through an additional low-pass (LP) LC filter to a Full-Bridge Converter (FBC) driven with 50% duty cycle so that it can be transformed into a square wave. The obtained alternating voltage is applied to a high-frequency transformer (HFT) with turn ratio $N = \frac{v_{it}}{v_{ot}} = 10$ for a further voltage reduction. The switching frequency of the IGBTs of the BC and FBC is 20 kHz.

Finally, the output voltage of the transformer is rectified by a diode full-bridge and then applied to the electrolyzer through another LC filter to obtain low current/voltage ripple at the switching frequency. It is worth noting that the resistors r_{L1}, r_{L2}, and r_{L3} represent the parasitic resistances of the inductors L_1, $L_2$and L_3 in the circuit model. Likewise, the resistors r_{C1}, r_{C2}, and r_{C3} represent the parasitic resistances of the capacitors C_1, C_2, and C_3. Finally, as justified in Section 2.2, the electrolyzer is modeled using a resistance R_{el} series-connected with a counter-electromotive force E_{el} in the circuit of Fig. 1.

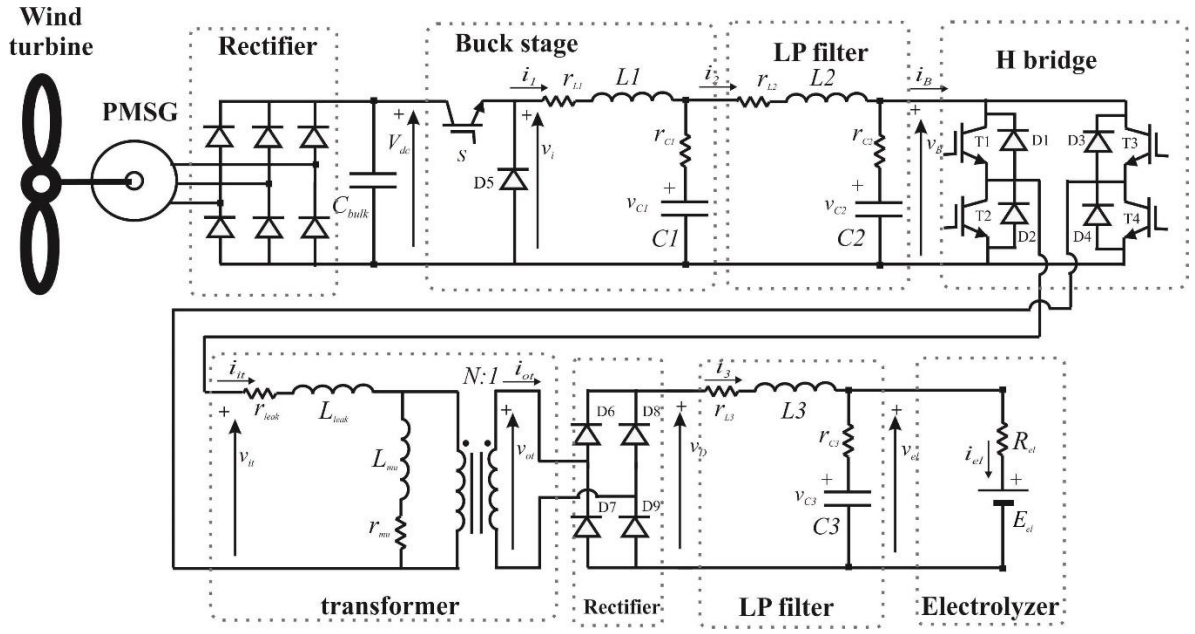

Fig. 1 Electric scheme of the system under study.

2.2 Mathematical model

The focus of the paper is on the electronic interface between the wind generator and the electrolyzer, i.e., the DC/DC converter. Hence, the dynamics of such devices are neglected, i.e., the wind generator and the electrolyzer are modeled as static devices. The input variable of the system is the DC voltage generated by the μWECS, whereas the output variable is the input voltage of the electrolyzer.

Since the wind generation process is controlled by means of a dedicated onboard controller, the set {turbine, generator, rectifier, bulk capacitor} is modeled as a variable voltage source, neglecting its dynamics. Consequently, also the DC voltage variation at the output of the rectifier is considered instantaneous, i.e., modeled as a step function. This situation represents the worst-case behavior, i.e., when the bulk capacitor has a low capacitance or is absent.

The electrolyzer is a very complex device, based on electrochemical processes that are very difficult to model. For this reason, the static electrical characteristics of the considered electrolyzer (i.e., voltage vs. current and power vs. current) have been experimentally acquired. The obtained characteristics are shown in Fig. 2. As the figure shows, the voltage vs. current characteristic is linear in the range of currents from about 3 A to 50 A, which is the usual operating range up to the rated power of the electrolyzer (~400 W, corresponding to $i_{el} = 50$ A and $v_{el} = 7.5$ V). Therefore, the electrolyzer is modeled as a resistance and a DC voltage source as described by the equation $v_{el} = R_{el} i_{el} + E_{el} = 0.0625 i_{el} + 4.375$. Both coefficients of the equation can be found by linearly interpolating the electrical characteristic in the range from about 3 A to 50 A.

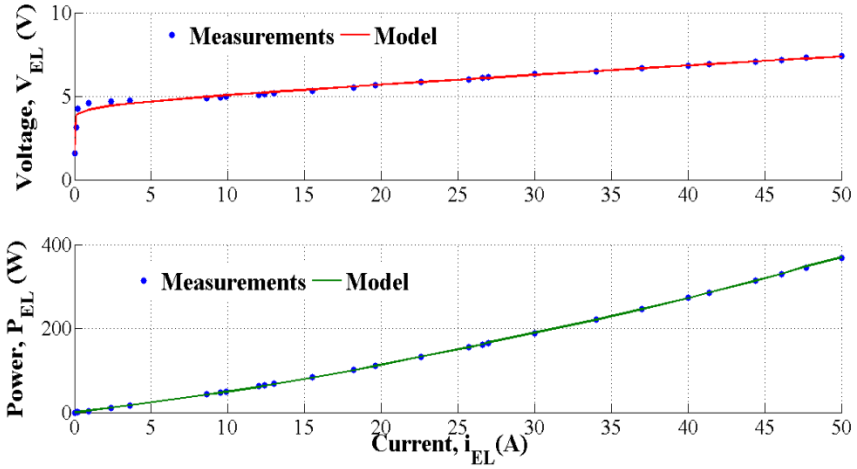

Fig. 2 Static characteristics of the considered electrolyzer.

As said, the plant under investigation in the present paper, shown in Fig. 1, represents the DC/DC converter that supplies an electrolyzer starting from the DC voltage generated by a μWECS. As for the construction of a mathematical model of the plant, different solutions exist depending on the intended use. If the model is to be used for simulation purposes, a detailed model can be constructed which takes into account almost all the phenomena occurring in the plant, including also the nonideality of the transformer (i.e., inductances and resistances describing the magnetization, leakage flux, and iron/copper losses of the transformer) and the commutation of the semiconductor devices present in the circuit. These two operating nonidealities are linked to each other. In fact, with reference to the DC/DC converter under investigation, shown in Fig. 1, if T_1 and T_4 are in the ON state and the gate signal is removed, the current will not go to

zero instantaneously due to the transformer nonideality. Similar behavior occurs at the secondary of the transformer, which is connected to a full-bridge diode rectifier. The commutation phenomena produce deviations of voltages and currents involved in the plant. The most significant effect on the circuit under study is the existence of zero-voltage intervals in the AC waveforms on both sides of the transformer, resulting in a non-negligible voltage drop of the rectified DC component at the input terminals of the LP filter placed before the electrolyzer.

Alternatively, it is possible to model the plant using models obtained through identification, i.e., on the basis of input-output sequences obtained experimentally during suitable tests performed on the system [27]-[28].

Another model which can be associated with the plant of Fig. 1 consists of a set of Linear and Time-Invariant (LTI) sub-models, each of which is operative in one of the possible conduction configurations of the semiconductor devices present in the circuit. For the plant under study, if the previously described commutation delays are neglected, at least four sub-models are needed. This modeling approach can be useful for control purposes as well as for simulation purposes if the design engineer wants to devise a control law in the context of hybrid systems [24].

If the model has to be used only for control design, then it must take into account only the most significant aspects of the system behavior, generally, those occurring at low frequency. Phenomena like those described above cannot be modeled. Instead, after constructing a model that is valid in the absence of commutation delays and considering an ideal transformer, a more accurate model can be constructed which globally takes into account the nonideality of the plant.

Starting from the circuit model of Fig. 1, in order to develop the mathematical model of the system under study, the parasitic resistances r_{L1}, r_{L2}, r_{C1}, and r_{C2} have been taken into account. Instead, for the sake of simplicity, the parasitic resistances r_{L3} and r_{C3} have been neglected. Furthermore, the high-frequency transformer has been considered ideal for the development of the mathematical model, i.e., its leakage and magnetizing inductances, together with the related resistances, have been neglected. In this way, the AC section of the circuit has no dynamics, and the DC current supplied to the electrolyzer can be obtained straightforwardly by multiplying the DC input current of the full-bridge for the transformer's turn ratio. This

choice allows considering only DC signals rather than taking into account the presence of alternating square waves; thus, an LTI model is obtained, in which all the variables are DC-type. The obtained model will be referred to in the following as the *ideal model*, and it is suitable to be used for designing the controller.

On the other hand, the transformer, the controlled H-bridge, and the diode rectifier work according to well-defined physical laws and give their contribution to the circuit operation. Therefore, the behavior of the ideal model can be different from that of the real circuit, especially at steady state, which is the most frequent operating condition of the plant. In order to overcome this problem and, at the same time, take advantage of the ideal model, an equivalent turn ratio N_{eq} (slightly higher than the real turn ratio N) is considered to account for the zero-voltage intervals in the AC waveforms and the resulting DC voltage drop. The equivalent turn ratio N_{eq} is chosen to minimize the deviation between the static characteristics of the ideal model with parameter N_{eq}, instead of N, and those of real plant. The method to obtain the equivalent turn ratio starting from the real turn ratio is shown in Section 2.3.

The equations of the model can be obtained using the State Space Averaging (SSA) technique [30]-[32], which involves defining a plant model for all the possible switching configurations and computing the weighted average among all the models as a function of the duty cycle of the gate signal.

Referring to the ideal model, the possible switching configurations of the plant under study are four, and they can be described referring to Fig. 3. It is worth highlighting that the difference between Fig. 1 and Fig. 3 is only the presence/absence of the components that take into account the nonideality of the transformer and the parasitic resistances of filter L_3C_3.

The output voltage of the additional LC filter cascaded to the BC, v_B, and the corresponding output current i_B are always positive because the BC is operating in CCM. Therefore, denoting the voltage from the cathode to the anode of diode D_5 as v_i, the following considerations can be made [14]:

1) According to Fig. 3a, when the switch S is in the ON state and T_1 and T_4 are in the ON state, we have $v_i = V_{dc}$, the voltage at the primary of the transformer is $v_{it} = v_B$, and it is positive; the voltage $v_{ot} = \frac{v_{it}}{N_{eq}}$ at the secondary is positive too and, consequently, the diodes D_6 and D_9 are ON.

Then, the current $i_{ot} = N_{eq} i_{it} = N_{eq} i_B$ and it is positive. Note that the current flowing through L_3 is given by $i_3 = i_{ot}$.

2) According to Fig. 3b, when the switch S is in the ON state and T_2 and T_3 are in the ON state, we still have $v_i = V_{dc}$, but now it is $v_{it} = -v_B$; the voltage at the secondary is also negative, and consequently the diodes D_7 and D_8 are ON; then, the current $i_{ot} = N_{eq} i_{it} = -N_{eq} i_B$ and it is negative because $i_{it} < 0$. However, the current flowing through L_3 is still positive and given by $i_3 = -i_{ot}$.

3) When the switch S is in the OFF state and T_1 and T_4 are in the ON state, the same considerations as in 1 apply, except that $v_i = 0$.

4) When the switch S is in the OFF state and T_2 and T_3 are in the ON state, the same considerations as in 2 apply, except that $v_i = 0$.

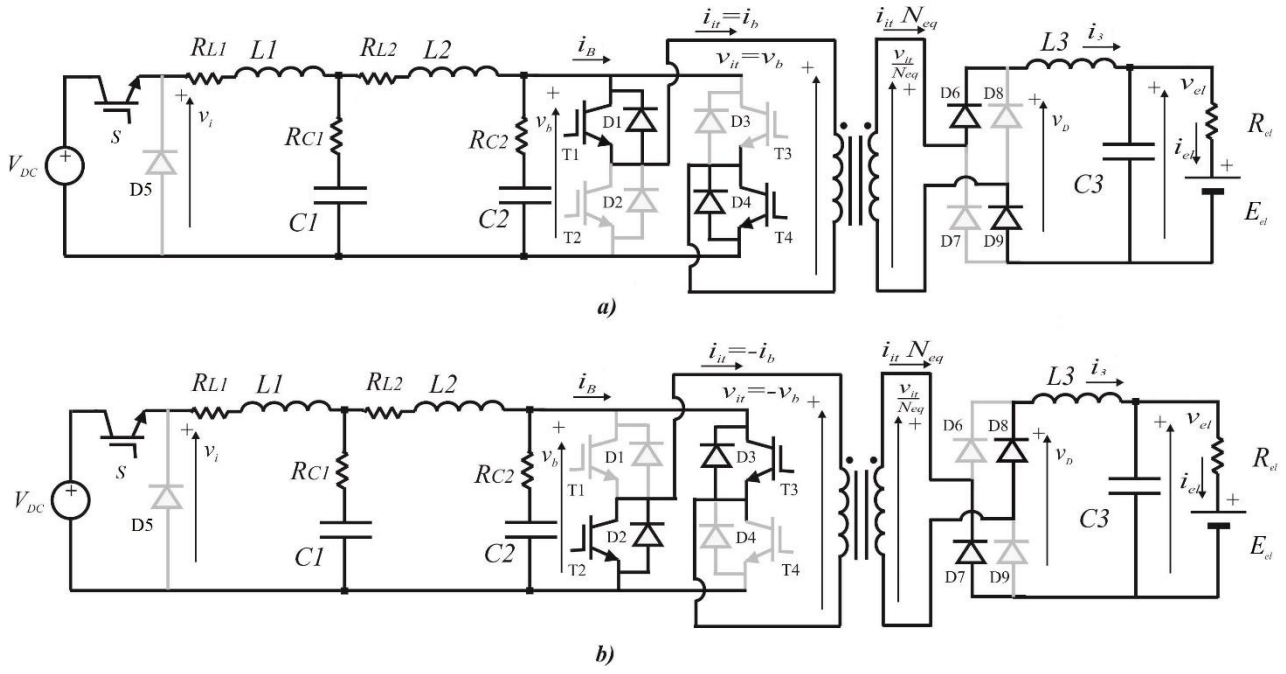

Fig. 3 Current flows in the ideal model in the situations described in 1) and 2), respectively

In order to develop the plant model, it is worth noting that the forcing input variables are V_{dc} and E_{el}, so the input vector is $u = [V_{dc} \quad E_{el}]^T$. The state variables are the currents flowing through the inductors L_1, L_2 and L_3 (namely i_1, i_2, and i_3) and the voltages on the capacitors C_1, C_2 and C_3 (namely v_{C1}, v_{C2} and v_{C3}). Then, the state vector is $x = [i_1 \quad i_2 \quad v_{c1} \quad v_{c2} \quad i_3 \quad v_{c3}]^T$. Since the parasitic resistance of the output

capacitor C_3 is neglected, the voltage v_{C3} is also the input voltage of the electrolyzer; therefore, the output of the system to be controlled is $y = v_{c3}$.

It is easy to verify that the differential equations describing the circuit of Fig. 1 when *S* is ON, i.e., in the situations considered in 1) and 2), are given in matrix form by:

$$\dot{x} = A_{ON}x + B_{ON}u \tag{1}$$

$$y = c_{ON}^{T}x \tag{2}$$

where:

$$A_{ON} = \begin{bmatrix} -\frac{r_{L1}+r_{C1}}{L_1} & \frac{r_{C1}}{L_1} & -\frac{1}{L_1} & 0 & 0 & 0 \\ \frac{r_{C1}}{L_2} & -\frac{r_{L2}+r_{C1}+r_{C2}}{L_2} & \frac{1}{L_2} & -\frac{1}{L_2} & \frac{r_{C2}}{N_{eq}L_2} & 0 \\ \frac{1}{C_1} & -\frac{1}{C_1} & 0 & 0 & 0 & 0 \\ 0 & \frac{1}{C_2} & 0 & 0 & -\frac{1}{N_{eq}C_2} & 0 \\ 0 & \frac{r_{C2}}{N_{eq}L_3} & 0 & \frac{1}{N_{eq}L_3} & -\frac{r_{C2}}{{N_{eq}}^2L_3} & -\frac{1}{L_3} \\ 0 & 0 & 0 & 0 & \frac{1}{C_3} & -\frac{1}{R_{el}C_3} \end{bmatrix}, \; B_{ON} = \begin{bmatrix} \frac{1}{L_1} & 0 \\ 0 & 0 \\ 0 & 0 \\ 0 & 0 \\ 0 & 0 \\ 0 & \frac{1}{R_{el}C_3} \end{bmatrix},$$

$c_{ON}^{T} = [0 \quad 0 \quad 0 \quad 0 \quad 0 \quad 1]$.

Similarly, the model corresponding to *S* in the OFF state (i.e., to the situations described in 3) and 4)), is given by:

$$\dot{x} = A_{OFF}x + B_{OFF}u \tag{3}$$

$$y = c_{OFF}^{T}x \tag{4}$$

where $A_{OFF} = A_{ON}$, $c_{OFF}^{T} = c_{ON}^{T}$, and:

$$B_{OFF} = \begin{bmatrix} 0 & 0 \\ 0 & 0 \\ 0 & 0 \\ 0 & 0 \\ 0 & 0 \\ 0 & \frac{1}{R_{el}C_3} \end{bmatrix}.$$

As it is well known, the control variable of the BC, thus of the whole system of Fig. 1, is the duty-cycle $d = \frac{t_{ON}}{T_{sw}}$, where t_{ON} is the time interval in which *S* is in the ON state, and T_{sw} is the switching period of the

PWM controller. Therefore, the average plant behavior is described by the following averaged state-space model [30]-[32]:

$$\dot{x} = Ax + Bu \tag{5}$$

$$y = c^T x \tag{6}$$

where:

$$A = A_{OFF} + (A_{ON} - A_{OFF})d = A_{OFF}$$

$$B = B_{OFF} + (B_{ON} - B_{OFF})d$$

$$c^T = c^T_{OFF} + (c^T_{ON} - c^T_{OFF})d = c^T_{OFF}$$

The model (5)-(6) is LTI, with state x and control variable d; the term $B_{OFF}u$ can be considered as a disturbance, and $(B_{ON} - B_{OFF})u$ is the matrix of the control gains. This result is typical of the Buck DC/DC converter. Instead, other types of DC/DC converters described in the average state-space present a nonlinear model. Finally, it is worth noting that, since the transformer is considered ideal, it is:

$$v_D = \frac{1}{N_{eq}} v_B \tag{7}$$

where v_D is the output voltage of the diode bridge.

2.3 Computation of the equivalent turn ratio

As stated before, an ideal model of the system (i.e., with an ideal transformer) is considered to avoid the hurdle implied by the simultaneous presence of both DC and alternating currents. However, an equivalent turn ratio N_{eq} must be assumed for the ideal transformer to let the ideal model behave as closely as possible to the real model, despite the absence of the neglected components. The following considerations must be made in order to compute the equivalent turn ratio N_{eq}. First, the static characteristics (electrolyzer voltage/current vs. duty cycle) of the converter operating at the nominal voltage V_{dc} are computed by simulating the real model in the PLECS environment. The obtained results are shown in Fig. 4 using black lines. The duty cycle spans a range that is defined by:

- a value that is slightly higher than the minimum duty-cycle that leads to CCM operation: $d_{min} = 0.291$;
- a value corresponding to the rated voltage (7.5 V) and current (50 A) of the electrolyzer: $d_{max} = 0.460$.

The average duty cycle in such a range is d^*=0.375 and, in this operating condition, we have $v_{el}{}^* = 6.333\ V$, $i_{el}{}^* = 31.4\ A$, and $v_B{}^* = 74.69\ V$ for the real model.

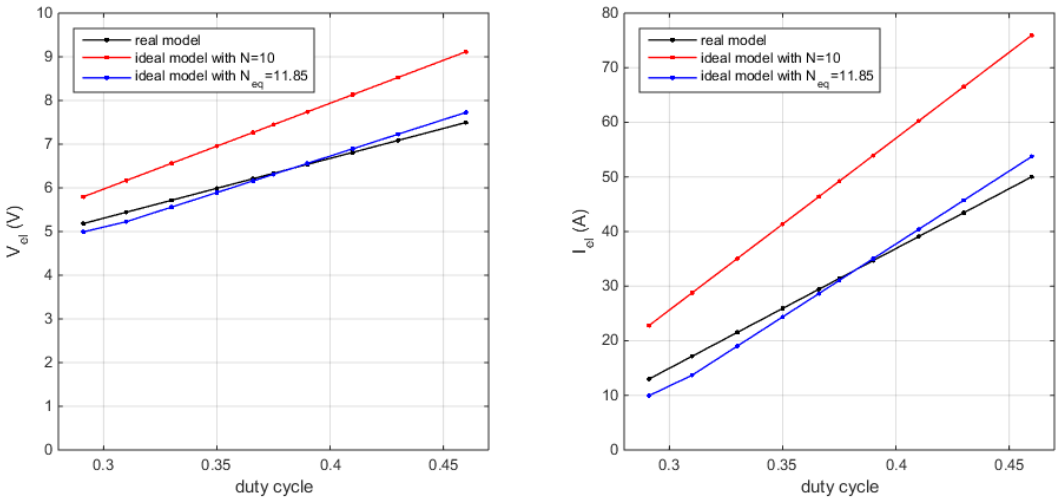

Fig. 4 Static characteristics of the converter: electrolyzer voltage vs. duty cycle (left); electrolyzer current vs. duty cycle (right).

Then, the static characteristics of the ideal model with the original turn ratio N of the transformer are computed. The results are plotted in Fig. 4 using red lines and show a significant deviation, as expected. The static characteristic of the real plant and that of the ideal plant can be made coincident at the average duty cycle d^* if the transformer's turn ratio allows obtaining the same electrolyzer voltage $v_{el}{}^*$ given the same voltage $v_B{}^*$ at the input of the full bridge. Since the voltage drop on the inductor L_3 is null in terms of DC values, it is possible to say that $v_D{}^* = v_{el}^*$. Then, substituting $v_D{}^*$ and v_B^* in the inverse of (7), it is possible to compute the equivalent turn ratio as:

$$N_{eq} = \frac{v_B{}^*}{v_D{}^*} = 11.85. \tag{8}$$

The static characteristics computed simulating the ideal model with the equivalent turn ratio N_{eq} are given in Fig. 4 using blue lines; they show a perfect match at d^* and acceptable deviations approaching the upper and lower bound of the considered duty cycle range, as expected.

3. DESIGN OF THE CONTROLLER

As a preliminary step to designing the controller for the system under study, it is convenient to put the model (5)-(6) in standard form. To this end, we define the equilibrium state of this model, corresponding to the constant input u and a duty cycle d^*, as the state x^* which satisfies the equation:

$$0 = A_{OFF}x^* + B_{OFF}u + (B_{ON} - B_{OFF})ud^* \tag{9}$$

Since the matrix A_{OFF} is invertible, this state surely exists and is given by:

$$x^* = -A_{OFF}^{-1}[B_{OFF}u + (B_{ON} - B_{OFF})ud^*] \tag{10}$$

Denoting by $\tilde{x} = x - x^*$ the perturbed state variable, the model of the system can be put in standard form:

$$\dot{\tilde{x}} = A\tilde{x} + b\tilde{d} \tag{11}$$

$$\tilde{y} = c^T\tilde{x} \tag{12}$$

in which $\tilde{d} = d - d^*$ is the perturbed control variable, $b = (B_{ON} - B_{OFF})u$, and $\tilde{y}$ is the perturbed output, i.e. the output referred to the equilibrium output c^Tx^*.

3.1 Controller design using classical frequency domain techniques

The transfer function of the model (11)-(12) is given by:

$$G_p(s) = K_p \frac{(s-z_1)(s-z_2)}{(s-p_1)(s-p_2)(s-p_3)(s-p_4)(s-p_5)(s-p_6)} \tag{13}$$

where:

$$K_p = 8.651 \times 10^{13},\ z_1 = -3.125 \times 10^6,\ z_2 = -1.93 \times 10^4,\ p_1 = -2.845 \times 10^5,$$
$$p_2 = -640 - j23680,\ p_3 = \overline{p_2},\ p_4 = -1150,\ p_5 = -100 - j1310,\ p_6 = \overline{p_5}$$

The poles of $G_p(s)$ are coincident with the eigenvalues of matrix A; therefore, the model (11)-(12) is controllable and observable, and $G_p(s)$ completely describes the system under study. This condition can be verified starting from the state-space model (11)-(12) and computing the determinant of the controllability matrix in terms of the electrical parameters using the Symbolic Math Toolbox of Matlab. The determinant of the controllability matrix is always non-null regardless of the electrical parameters, but its value is as high as 10^{92}. On the other hand, the determinant of the inverse of the controllability matrix, computed symbolically in terms of the electrical parameters, is as low as 10^{-110}. This result shows that the model of the system under study is numerically ill-conditioned. In fact, computing the controllability matrix numerically using Matlab, it appears that the controllability matrix has rank 3. The same result is obtained for the observability property. The above analysis shows that it is difficult to control the system under study, and it excludes the possibility of applying pole assignment techniques and the use of state observers.

3.2 Integral Controller

By looking at the transfer function (13), it can be noticed that this function has two couples of complex conjugate poles with damping ratio of 0.08 and 0.027, respectively. The analysis of the Bode diagrams of function $G_p\,(s)$ reveals the instability of the closed-loop system constructed around it due to the first resonance peak occurring at about 1310 rad/s. This analysis is carried out with the aim of understanding which controller and control methodology can be used to obtain a stable and well-performing closed-loop system. Besides achieving a type 1 closed-loop system, thus obtaining zero steady-state error in the presence of step reference signals, it is desired to attenuate the effects of this resonance, thus gaining stability of the closed-loop system. In order to achieve both goals, it is enough to introduce an integral action. The Bode diagram of the function $G_{p1}(s) = G_p(s)/s$ is shown in Fig. 5. Assuming that it is desired to have a crossover frequency of 100 rad/s, and phase and gain margins of at least 60 degrees and 10 dB, respectively, it results that a gain $K_c = 5.9$ (15.5 dB) must be added to $G_{p1}(s)$ to satisfy the above requirements. From Fig. 5, it can be inferred that the unit-feedback closed-loop system exhibits a phase margin of 84.5 degrees at a crossover frequency of 100 rad/s and a gain margin of 11.6 dB. Furthermore, it can be deduced that a higher value of K_c increases the crossover frequency and, thus, the bandwidth of the closed-loop system, but reduces the phase and gain margins.

For the system under study, the gain margin exhibited by the unit-feedback closed-loop system having $K_c G_{p1}(s)$ as the open-loop transfer function is not adequate for the robustness of stability. In fact, the magnitude of the above open-loop function at the resonance peak frequency is about -10 dB. Therefore, the closed-loop model is near to the instability with respect to the distance measured by the gain margin.

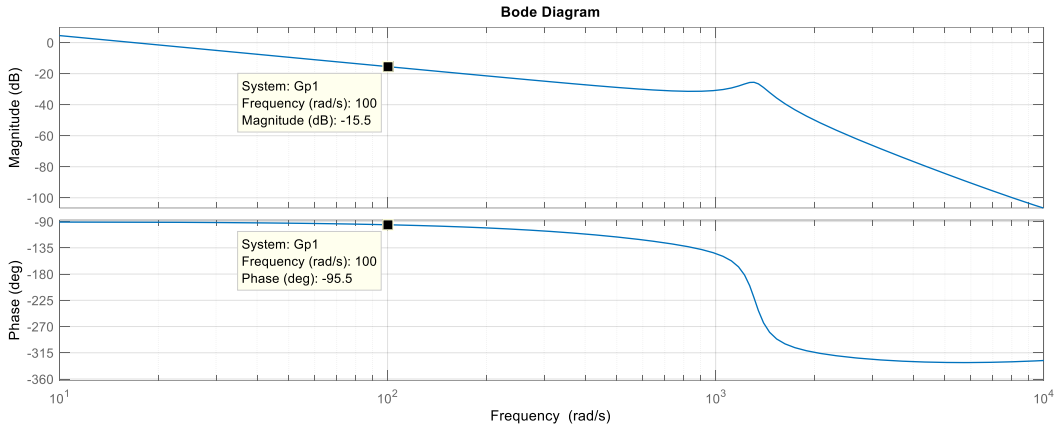

Fig. 5 Bode plot of $G_{p1}(j\omega)$

This integral-type controller has been implemented in the PLECS environment, and simulations have been performed to assess the dynamic behavior of the controlled system in several conditions. On the one hand, besides varying the output voltage reference $V_{el,ref}$, wide step variations of DC-link voltage V_{dc} have also been considered to reproduce the effect of fast fluctuations of wind speed. On the other hand, the presence of a low-frequency ripple superimposed to the DC link voltage has been contemplated. In fact, this ripple component is always present in the output voltage of a μWECS because it depends on the passive rectification stage. Its frequency is proportional to the angular speed of the wind turbine, which is about 10-25 rad/s for typical gearless μWECSs [25]; its amplitude, instead, depends on the capacitance C_{bulk} of the scheme in Fig. 1 and is a few percent of the average rectified voltage value. In the performed simulations, the low-frequency ripple has been modeled by superimposing a non-negligible sinusoidal component to the DC link voltage source modeling the whole μWECS; the amplitude of such a component has been set to ±4% of $V_{dc,rated}$, i.e., ±8 V, and a frequency of 76.4 Hz has been chosen, corresponding to a generator with 8 pole pairs rotating at 10 rad/s.

The following sequence of transients has been considered: the converter is turned on with $V_{dc} = 200\,V$ and an output voltage reference $V_{el,ref} = 7.5\,V$; at t=0.1 s, the setpoint is decreased to 6 V with a step

variation, and it is increased again to 7.5 V at t=0.2 s; at t=0.3 s, a step variation of DC-link voltage occurs, i.e., from 200 V to 150 V; finally, at t=0.4 V, the DC link voltage is increased from 150 V to 220 V, again with a step variation.

The simulation results are plotted in Figs. 6 and 7. As the figures show, without considering the low-frequency ripple, a satisfying behavior is obtained against step variations of output voltage reference $v_{el,ref}$ at rated DC link voltage $V_{dc,rated}$, i.e., until t=0.3 s. However, the behavior is not satisfactory for step variations of DC link voltage at constant output voltage reference, with severe over/undershoots. Furthermore, the situation worsens when the presence of the low-frequency ripple component superimposed to the DC supply is considered. The frequency of such a component is not much higher than the bandwidth of the closed-loop system, so it affects the output voltage and current consistently. As a matter of fact, the presence of such a low-frequency component has a detrimental effect on the electrolyzer lifespan and should be avoided.

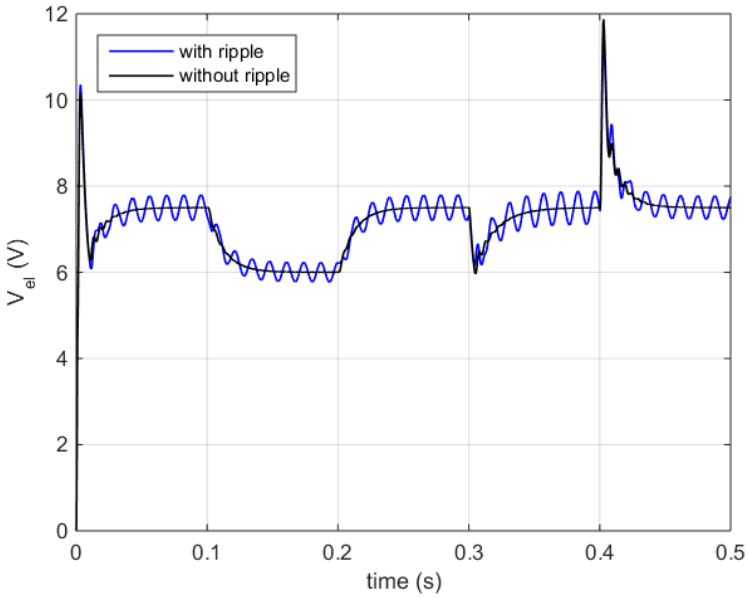

Fig. 6 Closed-loop response using integral-type controller: electrolyzer voltage

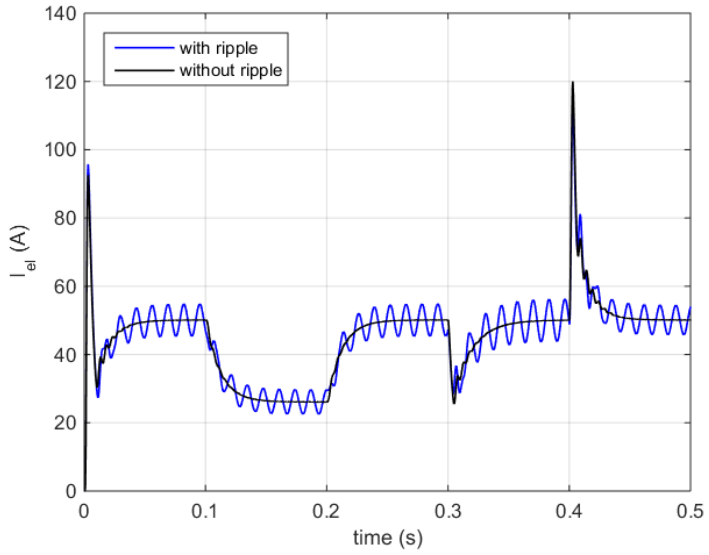

Fig. 7 Closed-loop response using integral-type controller: electrolyzer current

The obtained results can be explained considering that the task of the integral controller is only to allow achieving zero steady-state error when a step reference signal is applied to the closed-loop system. Such a controller cannot ensure the maintenance of the stability property and good behavior in the presence of parameter variations and unmodelled dynamics in the plant. In order to cope with these drawbacks, robust control techniques have to be employed. As for the case study considered in this paper, the use of robust control techniques is justified also from the pole-zero portrait of the transfer function $G_p(s)$. As already said, this function has two couples of complex conjugate poles with very low damping, and the system is difficult to control using conventional control techniques. On the other hand, robust control techniques consist in: 1) defining a nominal model obtained assuming the nominal values of the parameters, and neglecting the high frequency dynamics of the plant under study; 2) designing a robust controller for the nominal model, able to cope with uncertainties consisting of the unmodelled dynamics and/or parameter deviations [26], [29] . Then, in this paper robust control techniques are employed for a nominal model having only the poles and zeros of $G_p(s)$ lying in convenient locations on the complex s-plane, that are suitable for the controller design. Instead, a transfer function containing the remaining poles and zeros of the transfer function $G_p(s)$ with very low damping is considered as unmodeled dynamics [27]-[28].

3.3 Controller design using robust control techniques

The control technique employed for designing a controller for the system under study is that of robust control in the frequency domain [26]. According to this method, the model of the system under study is defined as a member of the following set:

$$\mathcal{G}_p = \left\{ G_p(s): \left| \frac{G_p(j\omega) - G_{pn}(j\omega)}{G_{pn}(j\omega)} \right| \leq \Delta_m(\omega),\ \forall \omega \geq 0 \right\}, \tag{14}$$

where $G_{pn}(s)$ is the nominal transfer function of the system under study, and $\Delta_m(\omega)$ is the uncertainty in the knowledge of the model.

The first step is the choice of the nominal model so that it is physically realizable and reproduces the low-frequency performance of the system, including the steady-state. In terms of the transfer function, the nominal model contains the dominant poles, some zeros on the left half-plane, and the gain of the full model. The poles with very low damping coefficients, which are very difficult to treat, are confined into the unmodelled dynamics. The robust control will take care of these dynamics and of parametric uncertainties as well.

For the given system under study, the nominal model is chosen as follows:

$$G_{pn}(s) = K_{pn} \frac{s - z_2}{(s - p_4)(s - p_5)(s - p_6)}, \tag{15}$$

in which K_{pn} is chosen so that $G_{pn}(s)$ has the same gain as (13). The remaining poles and zeros are associated with a function $G_{pi}(s)$ that is defined as unmodelled dynamics. In this way, the poles that are far from the imaginary axis and those having very low damping ratio contribute to the controller design only indirectly, i.e., they do not contribute to the structure of the controller. Instead, they contribute to the determination of its parameters so that the desired robustness property is achieved. This approach dramatically simplifies the controller design process.

The transfer function $G_{pi}(s)$ is given by:

$$G_{pi}(s) = K_{pi} \frac{s - z_1}{(s - p_1)(s - p_2)(s - p_3)}, \tag{16}$$

where $K_{pi} = K_p/K_{pn}$. In order to define the uncertainty, bound $\Delta_m(\omega)$ for (14), the function $\Delta(s)$ is first computed as:

$$\Delta(s) = \frac{G_p(s) - G_{pn}(s)}{G_{pn}(s)} = G_{pi}(s) - 1. \tag{17}$$

Then, $\Delta_m(\omega)$ is a real and non-decreasing function of ω, which satisfies the inequality $\Delta_m(\omega) \geq |\Delta(j\omega)|, \forall\omega \geq 0$. In the case under study, $|\Delta(j\omega)|$ is plotted in Fig. 8, where resonance is evident at $\omega_r = 23700$ rad/s with a resonance peak $M_r = 25.4$ dB. In order to simplify the design of the controller, the disk representation of uncertainty is used here. To understand this representation, equation (14) is written as $\left|G_p(j\omega) - G_{pn}(j\omega)\right| \leq \Delta_m(\omega)\left|G_{pn}(j\omega)\right|,\ \forall\omega \geq 0$. This implies that the end of the vector $G_p(j\omega)$ can lay on any point inside the circumference that is centered at the end of the vector $G_{pn}(j\omega)$, in the Nyquist plane of the function $G_{pn}(j\omega)$, and has radius $\Delta_m(\omega)\left|G_{pn}(j\omega)\right|$. Since, as already said, $\boldsymbol{\Delta_m(\omega)}$ is a non-decreasing function of $\boldsymbol{\omega}$, if $|\Delta(\boldsymbol{j\omega})|$ has the shape of Fig. 8, it is necessary to define $\boldsymbol{\Delta_m(\omega)}$ as $\boldsymbol{\Delta_m(\omega) = |\Delta(j\omega)|}$ for $\boldsymbol{\omega \leq \omega_r}$ and $\boldsymbol{\Delta_m(\omega) = M_r}$ for $\boldsymbol{\omega > \omega_r}$.

As for the class of inputs to be considered for designing the controller, it is convenient to refer to smooth inputs as suggested by [27], i.e., those expressed by:

$$\tilde{Y}_{ref}(s) = \frac{\beta\gamma}{s(s+\beta)(s+\gamma)}. \tag{18}$$

Each of such inputs can be considered as the output of a transfer function $W_{in}(s) = \gamma\sqrt{\frac{\beta}{2}}\frac{1}{s(s+\gamma)}$ subject to the input $V(s) = \frac{\sqrt{2\beta}}{s+\beta}$, which is an input with bounded 2-norm, i.e., $\int_0^\infty |v(t)|^2 dt = 1$.

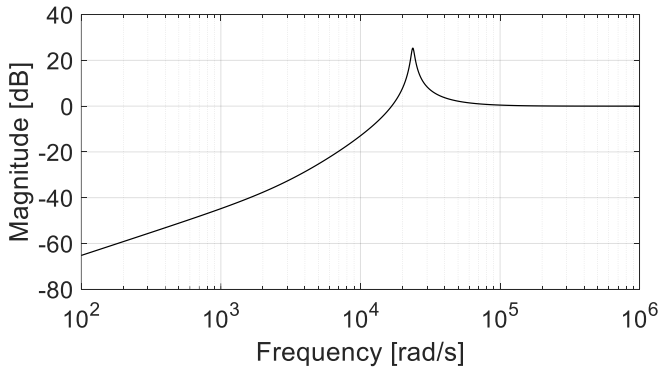

Fig. 8 Magnitude Bode diagram of $|\Delta(j\omega)|$ vs. ω.

The design of the controller will be carried out using the Internal Model Control (IMC) scheme given in Fig. 9, where $G_q(s)$ is the transfer function of the controller. This scheme is equivalent to the classical unit-feedback control scheme, in which the controller $G_c(s)$ is series connected to the plant $G_p(s)$, and the relationship between $G_q(s)$ and $G_c(s)$ is given by:

$$G_c(s) = \frac{G_q(s)}{1 - G_{pn}(s)G_q(s)}. \tag{19}$$

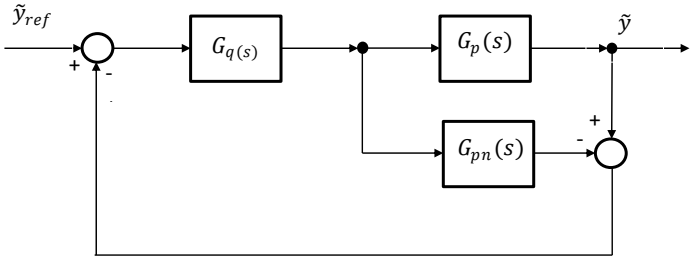

Fig. 9 IMC control scheme

In the following, first, the controller $G_q(s)$ will be designed, and then the controller $G_c(s)$ will be obtained using (19). A simplified procedure for designing $G_q(s)$ consists of the following steps:

a) a controller $G_{qn}(s)$ is designed so that the 2-norm of the error signal, $\tilde{e}_n(t) = \tilde{y}_{ref}(t) - \tilde{y}$, is minimized, assuming that $\tilde{y}_{ref}(t)$ is the specific input (18) and the plant transfer function is the nominal one, i.e., $G_p(s) = G_{pn}(s)$, regardless of whether the controller is proper or not;

b) an IMC filter having transfer function $G_f(s)$ is designed so that the controller $G_q(s) = G_{qn}(s)G_f(s)$ is physically realizable (i.e., stable and proper or strictly proper) and allows satisfying the robust behavior condition.

It is worth recalling that the robust behavior condition is given by:

$$\left|\tilde{S}_n(j\omega)W_{in}(j\omega)\right| + \left|\tilde{C}_n(j\omega)\Delta_m(\omega)\right| < 1, \forall\omega \geq 0\ , \tag{20}$$

where $\tilde{S}_n(j\omega) = 1 - G_q(j\omega)G_{pn}(j\omega)$ is the nominal sensitivity function (i.e., the link between the Fourier transforms of the error $\tilde{e}_n(t)$ and $\tilde{y}_{ref}(t)$, given by $\tilde{E}_n(j\omega) = \tilde{S}_n(j\omega)\tilde{Y}_{ref}(j\omega)$), and $\tilde{C}_n(j\omega) = 1 - \tilde{S}_n(j\omega) = G_q(j\omega)G_{pn}(j\omega)$ is the nominal complementary sensitivity function. The function $\Delta_m(\omega)$ defines

the uncertainty bound as shown in (14), whereas $W_{in}(s)$ depends on the class of reference inputs chosen for supplying the control system, and it is given above. It is worth noting that such a condition implies that of robust stability, which is given by $\left|\tilde{C}_n(j\omega)\Delta_m(\omega)\right| < 1, \forall\omega \geq 0$.

As for the design of $G_{qn}(s)$, practically, it can be performed by minimizing the ISE performance index according to:

$$\min_{G_{qn}} \int_0^\infty \tilde{e}_n^2(t)dt = \min_{G_{qn}} \frac{1}{2\pi}\int_{-\infty}^{+\infty}\left|\tilde{E}_n(j\omega)\right|^2 d\omega = \min_{G_{qn}} \frac{1}{2\pi}\int_{-\infty}^{+\infty}\left|\tilde{S}_n(j\omega)\tilde{Y}_{ref}(j\omega)\right|^2 d\omega. \quad (21)$$

Since $G_{pn}(s)$ is minimum-phase (no zeros on the right half-plane), the minimum of (21) is zero, and it is obtained for $G_{qn}(s) = \frac{1}{G_{pn}(s)}$. (22)

The controller $G_{qn}(s)$ is not physically realizable because the transfer function is improper. The sensitivity function corresponding to this controller is $\bar{S}(s) = 0$, which means that a step reference signal should be reproduced unchanged at the output. For these reasons, it is necessary to add a function $G_f(s)$ that produces a proper controller $G_q(s) = G_{qn}(s)G_f(s)$; the corresponding sensitivity function $\tilde{S}_n(s) = 1 - G_q(s)G_{pn}(s)$ has a zero at the origin, i.e., the closed-loop system is of type 1, which satisfies the condition of robust behavior (20). Note that $\tilde{S}_n(0) = 1 - G_f(0)$ because $G_{qn}(0)G_{pn}(0) = 1$; consequently, if $G_f(0) = 1$, the sensitivity function $\tilde{S}_n(s)$ has a zero at the origin. A possible structure of $G_f(s)$ is given by:

$$G_f(s) = \frac{\alpha_{m-1}s^{m-1}+\cdots+\alpha_1 s^m + a_0}{(1+\lambda s)^n}. \quad (23)$$

The structure (23) is not the unique structure able to satisfy the desired goals. However, it is particularly simple for the choice of its parameters [26]. In particular, m and the corresponding parameters $a_0, \ldots, a_{m-1}$ are chosen in order to satisfy the requirements on the type of the closed-loop system (type 1 implies zero steady-state error in the presence of step reference signals, type 2 implies null steady-state errors in the presence of step or ramp reference signals, and so on). The parameter *n* is chosen so that the transfer function of the controller is proper or strictly proper. Finally, the parameter λ is chosen so that the robust behavior condition (20) is satisfied.

It is worth noting that the controller $G_q(s)$ is designed for the IMC control scheme, but the whole control system is implemented according to the feedback control scheme in which the controller is $G_c(s)$. As already said, the relationship between the controllers $G_q(s)$ and $G_c(s)$ is given in (19). As it is easy to prove, the nominal sensitivity function and the nominal transfer function of the feedback control scheme (see Fig. 11), both computed for $G_p(s) = G_{pn}(s)$, are the same of those computed for the IMC control scheme of Fig. 9. Consequently, if $G_q(s)$ is a robust controller for the IMC system, then $G_c(s)$ is robust for the feedback control scheme. The robustness of $G_q(s) = G_{qn}(s)G_f(s)$ is shown verifying if it satisfies (20). Note that in (20) only the parameter λ is unknown, and the problem is to obtain the value of λ that satisfies (20) with a certain margin, and this can be made in a few steps. As it is easy to verify, the input-output transfer function of the designed closed loop control system is $W(s) = G_q(s)G_{pn}(s) = G_f(s)$, and its bandwidth is $1/\lambda$. It follows that the parameter λ has to be chosen with a trade-off between the dynamics of the closed loop system and the robustness margin. Increasing λ produces a reduction of the dynamics but an increase of the robustness margin.

In the case under study, $m = 1$, $a_0 = 1$, and $n = 2$ satisfy the condition of type 1 system and lead to a controller $G_q(s)$ that is proper regardless of λ. Choosing $\beta = 1300$, $\gamma = 3900$, and $\lambda = 0.0003$, the left-hand side (LHS) of (20) has the shape shown in Fig. 10; thus, the condition of robust behavior is satisfied with a good margin.

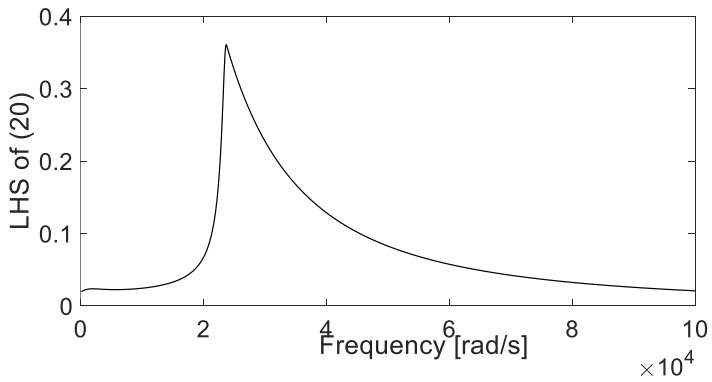

Fig. 10 LHS of (20) vs. ω.

Once the controller $G_q(s)$ has been designed, the controller $G_c(s)$ of the feedback control scheme can be computed using (19), obtaining the function:

$$G_c(s) = K_c \frac{(s-p_4)(s-p_5)(s-p_6)}{(s)(s-z_2)(s+2/\lambda)}. \tag{24}$$

where $K_c = 6.562$.

3.4 Implementation of the robust controller

The controller designed in the previous Subsection is inserted into the control loop, as indicated in Fig. 11. In this scheme, $\tilde{e}(t) = \tilde{y}_{ref}(t) - \tilde{y}(t) = y_{ref}(t) - y(t)$ and $\tilde{d}(t) = d(t) - d^*$. Consequently, the implementation of the controller for the system under investigation is the one shown in Fig. 12. Examination of the figure shows that the controller also gives a sort of feedforward action that is independent of the reference signal. This action derives from the modeling process of the plant aimed at obtaining a model in standard form.

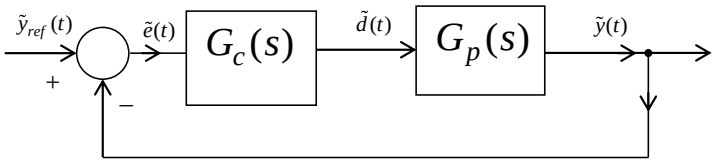

Fig. 11 Block scheme of the closed-loop control system

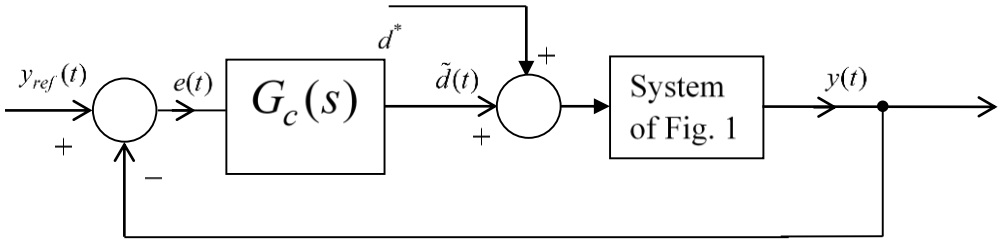

Fig. 12 Block scheme of the implemented controllers

3.5 Robustness Against DC-link Voltage Variations

As stated in Section 2.1, it is assumed that the DC/DC converter can be supplied by a voltage $V_{dc} \in [150, 220]$ V due to the usually wide fluctuations of wind energy. Consequently, it is necessary to prove the robustness of the designed controller against voltage variations in the said range. For a given control system, the robustness property against parameter variations or unmodelled dynamics is verified assessing whether the LHS of (20) is lower than one $\forall \omega \geq 0$. The evaluation of such a quantity is carried out in Matlab environment (or similar). It follows that the analysis of the robustness of behavior (which includes, as already said, that of stability) of the proposed controller that is carried out in this paper has a rigorous validity from a theoretical point of view, and it is not merely the result of a simulation process.

To this end, the transfer function of the system under investigation is computed for the lower and upper bounds values of V_{dc} denoted, respectively, by $G_{p150}(s)$ and $G_{p220}(s)$. Then, it is possible to compute the corresponding lower and upper bounds of uncertainties, denoted by $\Delta_{m150}(\omega)$ and $\Delta_{m220}(\omega)$, as follows:

$$\Delta_{ma}(\omega) = max \left| \frac{G_{pa}(j\omega) - G_{pn}(j\omega)}{G_{pn}(j\omega)} \right|, \forall \omega \;\; a \in \{150,220\} \tag{25}$$

Finally, it must be assessed whether the condition (20) is satisfied, substituting the functions $\Delta_{ma}(\omega)$ to $\Delta_m(\omega)$.

In the case under study, the functions $\Delta_{m150}(\omega)$ and $\Delta_{m220}(\omega)$ take the shape of Fig. 13, whereas the LHS of (20), computed as a function of ω for the above two values of V_{dc}, is shown in Fig. 14. Examination of Fig. 13 shows that the uncertainty increases with V_{dc}. Examination of Fig. 14 shows that, in the range of variation of V_{dc}, the condition of robust performance, and consequently that of robust stability, is satisfied with a large margin. For the sake of completeness, the peak values of the LHS of (20) corresponding to some increasing values of V_{dc} have been shown in Table I. Although the LHS of (20) increases with V_{dc}, the condition of robust behavior is satisfied with a large margin in the expected range of values of the DC-link voltage.

Table I. Peak of the LHS of (20) vs. variation of V_{dc}

V_{dc} **(V)**	150	175	200	220	250
Peak of the LHS of (20)	0.2710	0.3158	0.3610	0.3964	0.4502

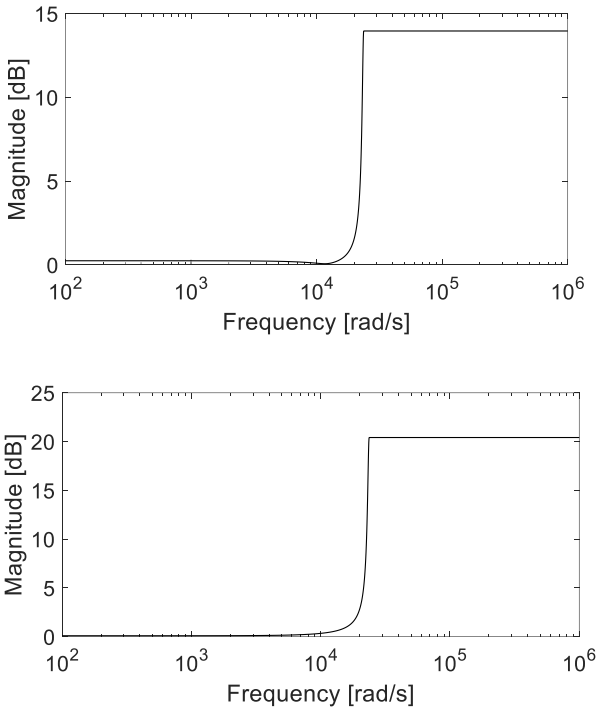

Fig. 13 Uncertainties for $V_{dc} = 150\,V$ and $V_{dc} = 220\,V$: shape of $\Delta_{m150}(\omega)$ (left); shape of $\Delta_{m220}(\omega)$ (right)

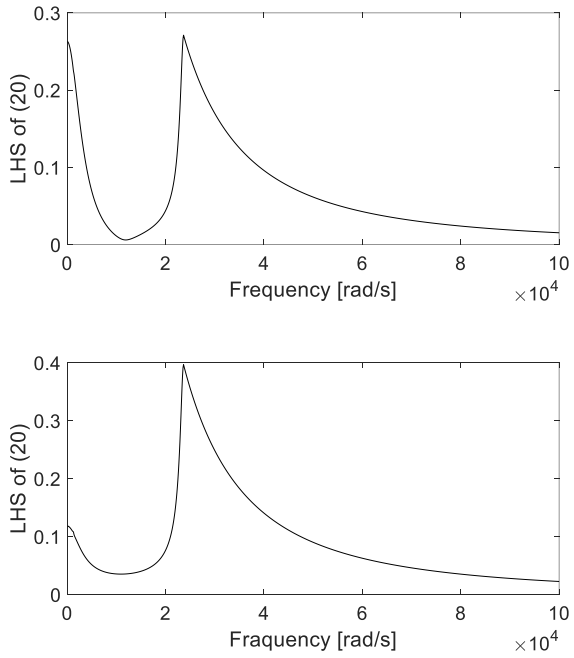

Fig. 14 LHS of (20) for lower and upper bounds of V_{dc}: $V_{dc} = 150$ V (upper); $V_{dc} = 220$ V (down)

3.6 Robustness against uncertainty in the buck inductance value

For the sake of completeness, it is worth assessing the robust behavior against the uncertainty in the knowledge of the inductance L_1 at the output of the buck converter, which is a critical component because of its rating (1.2 mH @ 5 A) [14]. Therefore, the peak values of the LHS of (20) have been evaluated for inductance deviations (ΔL_1) of $\pm 10\%$ and considering increasing values of the DC link voltage.

The results are summarized in Table II and show that robust behavior is maintained in all the considered situations. However, if large deviations are expected for this inductance, it is necessary to restrict the bandwidth of the closed-loop system by increasing λ.

Furthermore, analogous tests can be carried out considering the other electrical components of the converter, thus determining the largest set of parameter deviations that could produce the robustness loss of the controller.

Tab II. Peak of the LHS of (20) vs. variation of V_{dc} and deviations of L_1

Peak of the LHS of (20)	**V_{dc} (V)**				
	150	175	200	220	250
ΔL_1=+10%	0.425	0.427	0.430	0.470	0.575
ΔL_1=-10%	0.510	0.529	0.600	0.687	0.840

4. SIMULATION RESULTS

In order to test the robust controller designed in Section 3, it has been implemented in Matlab and connected to the physical model of Fig. 3 implemented in PLECS environment. Then, simulations have been performed considering the same sequence of transients of Section 3.1. The simulation results obtained without considering the low-frequency ripple are shown in Fig. 15, whereas Fig. 16 shows those obtained by taking into account such a disturbance.

According to Fig. 15, both controllers exhibit zero steady-state error and settle on the expected operating conditions, i.e., 50 A at 7.5 V (with d=0.46) and 26.1 A at 6 V (with d=0.35). Furthermore, with both controllers, the electrolyzer is properly supplied with a pure DC voltage, since the high-frequency ripple at the switching frequency (20 kHz) has been adequately filtered by the output LC filter. However, the

examination of Fig. 15 shows the difference between the two controllers and confirms the results obtained from the above robustness analysis. In particular, the dynamic performance of the robust controller is much higher than that of the integral-type controller, as reported in Table III. After the occurrence of either a reference voltage variation or a disturbance in the DC-link voltage, the robust controller is able to adapt to the new dynamic situation in few milliseconds; on the other hand, the integral controller is at least three times slower, especially in the presence of DC-link voltage variations. Moreover, for a disturbance in the DC-link voltage, the under/overshoots in the electrolyzer voltage and current are particularly large when the integral control is applied. In fact, using the robust controller, the voltage peak is reduced from 11.87 V to 8.37 V (i.e., -29.5%), whereas the current peak decreases from 120 A to 64 A (i.e., -46.7%).

Table III. Settling time at 5% computed for the waveforms of Fig. 15.

Time interval	Steady-state voltage	Integral-type controller	Robust controller	Deviation
0.1 s - 0.2 s	6 V	20.0 ms	7.2 ms	-64.4%
0.2 s - 0.3 s	7.5 V	17.2 ms	2.5 ms	-85%
0.3 s - 0.4 s	7.5 V	25.9 ms	2.8 ms	-89%
0.4 s - 0.5 s	7.5 V	21.0 ms	5.9 ms	-72%

As shown in Fig. 16, an additional outcome of the designed robust controller is that it significantly mitigates the low-frequency ripple (76.4 Hz) due to the presence of the rectification stage after the wind generator. Table IV reports the peak-to-peak amplitude of such a ripple on the electrolyzer side for the different waveforms of Fig. 16, highlighting the significant reduction obtained when the integral-type controller is replaced with the robust controller.

Table IV. Amplitude of low-frequency ripple in the waveforms of Fig. 16.

Time interval	Steady-state voltage	Integral-type controller	Robust controller	Deviation
0.1 s - 0.2 s	6 V	453 mV_{pp}	161 mV_{pp}	-64.4%
0.2 s - 0.3 s	7.5 V	587 mV_{pp}	225 mV_{pp}	-61.7%
0.3 s - 0.4 s	7.5 V	788 mV_{pp}	317 mV_{pp}	-59.8%
0.4 s - 0.5 s	7.5 V	551 mV_{pp}	196 mV_{pp}	-64.4%

Finally, the robust controller also helps to reduce the initial voltage and current peaks that occur when the DC/DC converter is turned on, thus limiting the stress on the electrical components. In particular, the initial voltage peak is reduced from 10.1 V to 8.9 V (i.e., -11.9%), whereas the corresponding current peak decreases from 92.4 A to 72.4 A (i.e., -21.6%).

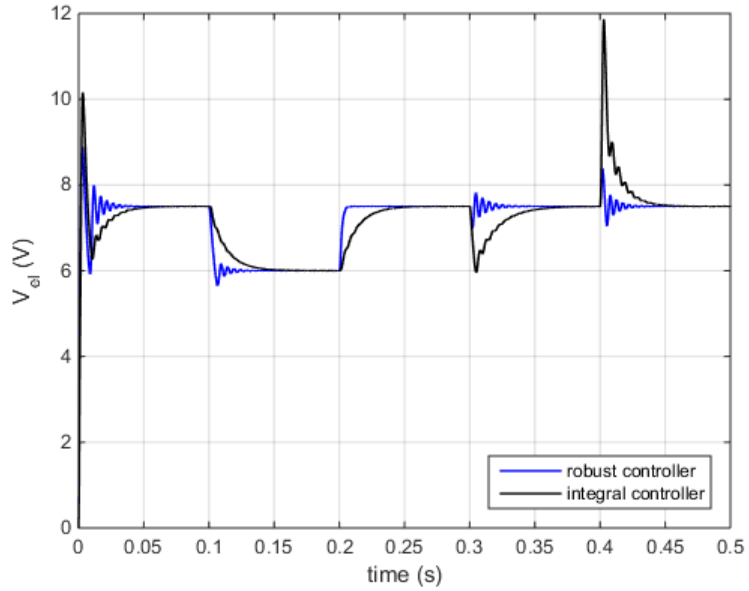
12
10
8
6
4
2
0
V_{el} (V)
0
0.05
0.1
0.15
0.2
0.25
0.3
0.35
0.4
0.45
0.5
time (s)
robust controller
integral controller

a)

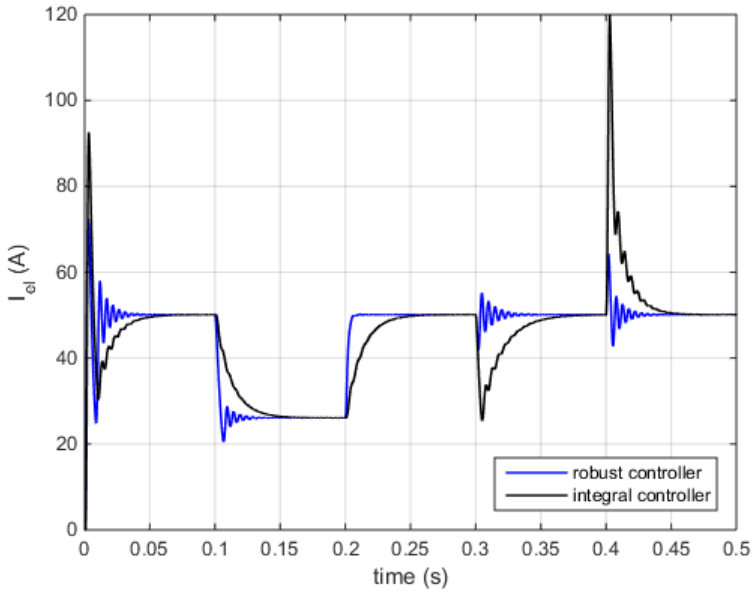
120
100
80
60
40
20
0
I_{el} (A)
0
0.05
0.1
0.15
0.2
0.25
0.3
0.35
0.4
0.45
0.5
time (s)
robust controller
integral controller

b)

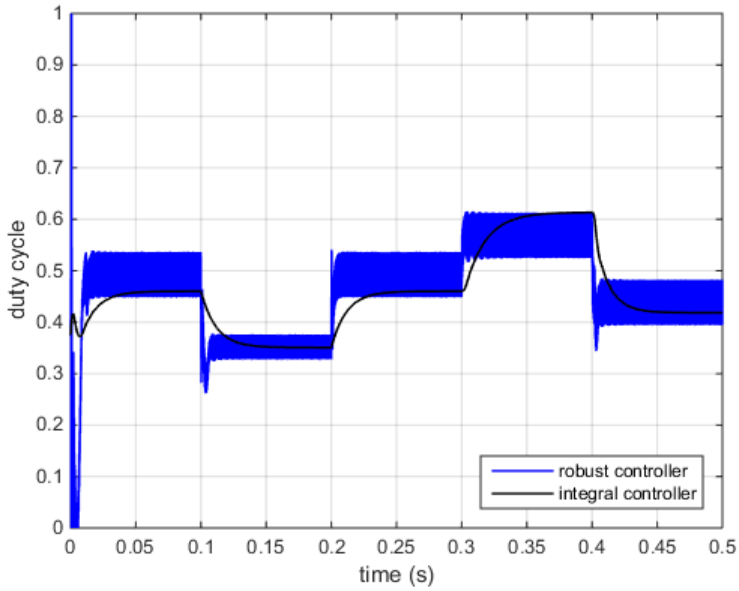

c)

Fig. 15 Simulation results with integral and robust controllers without considering DC-link ripple: a) electrolyzer voltage; b) electrolyzer current; c) duty cycle.

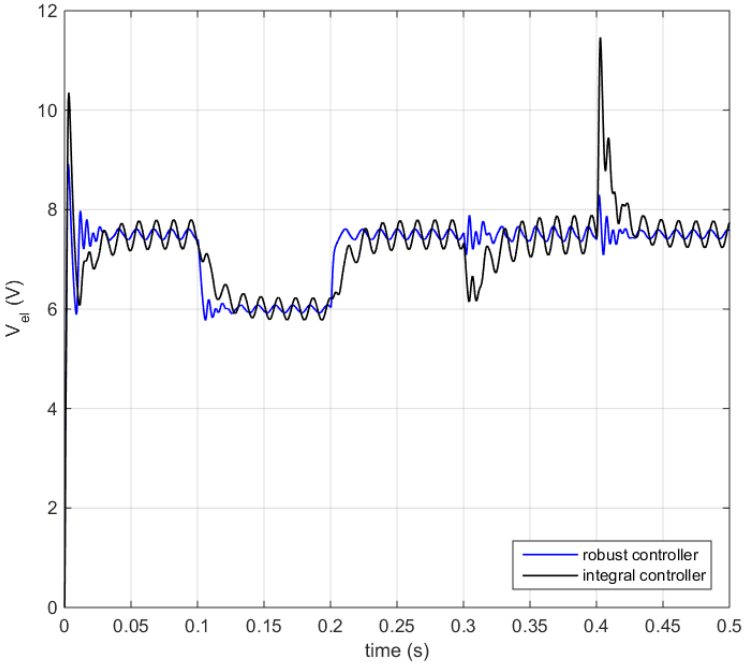

a)

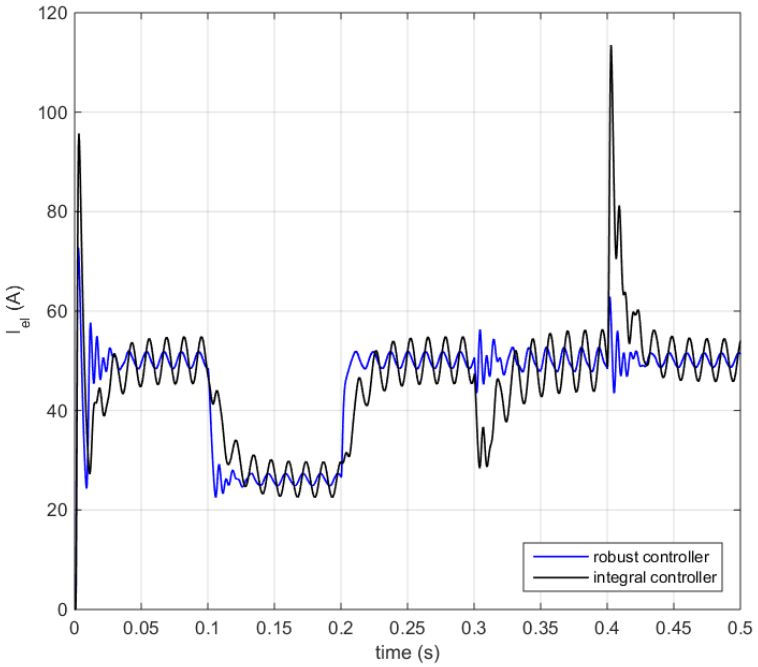

b)

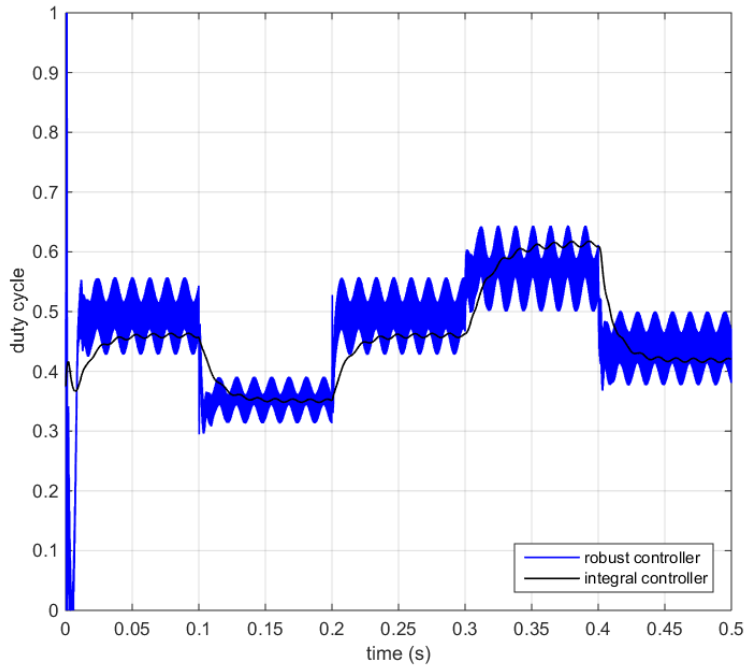

c)

Fig. 16 Simulation results with integral and robust controllers considering DC-link ripple: a) electrolyzer voltage; b) electrolyzer current; c) duty cycle.

5. EXPERIMENTAL VALIDATION

5.1 Description of the test bench

A suitable test bench has been set up to compare the performance exhibited by the integral and robust controllers in two scenarios: a) for step variations of reference output voltage; b) for step variations of input voltage. Such a test bench is depicted in Fig. 17, and it is made up of the following components replicating the scheme of Fig. 1: a TDK-Lambda GEN600-5.5 power supply that can be programmed using Labview; a first SEMISTACK-IGBT module used as a three-phase diode rectifier and buck converter; a double stage LC filter; a second SEMISTACK-IGBT used as a full-bridge converter and single-phase diode bridge; a high-frequency transformer model CEFEM 47/17/001 TFO 800W 20kHz with 10:1 turn ratio; an LC output filter; a Heliocentris NMH2-1000 PEM electrolyzer with its water tank; suitable voltage/current sensors and laboratory instrumentation; a dSPACE 1103 board and the related control desk to implement the control algorithms under test and the PWM modulators for the buck and full bridge converters. The voltage and current waveforms are acquired by means of an Agilent MSO6104A 4 Gsamples/s oscilloscope that allows saving both the screenshot and the sampled data file.

The developed test bench allows to manage a maximum output power of about 70 W at an operating point around 5.3 V and 12.5 A, taking into account the resistance of the connecting cables and connectors (11.5 mΩ).

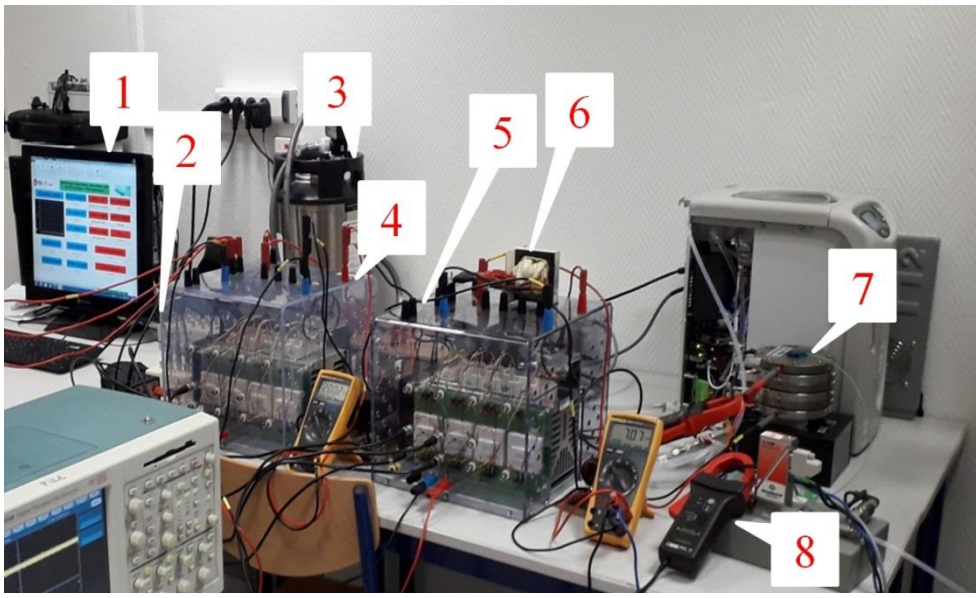

Fig. 17. Developed experimental test bench: 1) dSPACE control desk, 2) dSPACE board, 3) de-ionized water tank, 4) SEMISTACK-IGBT (three-phase diode rectifier and buck converter), 5) SEMISTACK-IGBT (full-bridge converter), 6) high-frequency transformer, 7) proton exchange membrane electrolyzer, 8) PAC10 current clamp.

5.2 Response to set-point variation

For each controller, a set-point variation has been applied, i.e., from 5 V to 5.3 V and vice versa, when the whole system is supplied at its nominal input voltage level (200 V DC). The current and power levels corresponding to 5 V are 8.5 A and 42.5 W, respectively. The obtained output voltage and current are shown in Fig. 18. It is worth noting that the

influence of the inherent switching noise is heavier on the output voltage, due to the low signal level. Therefore, it is more convenient to evaluate the current waveforms. For each transient direction, the acquired current waveforms have been imported in Matlab and plotted superimposed on the same graph, as shown in Fig. 19.

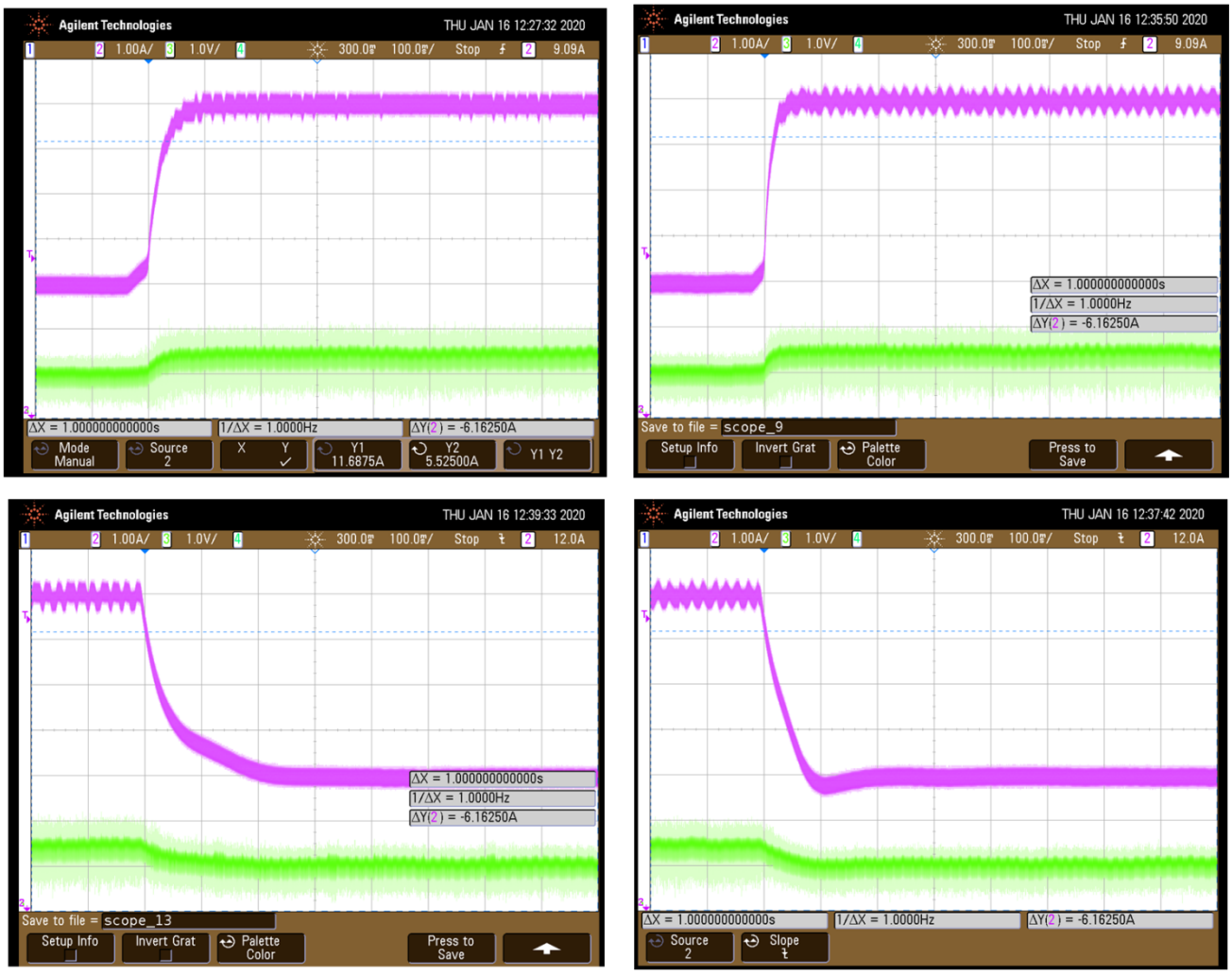

Fig. 18. Output voltage (green) and current (purple) transient after step set-point variation: from 5 V to 5.3 V with integral controller (upper left); from 5 V to 5.3 V with robust controller (upper right); from 5.3 V to 5 V with integral controller (lower left); from 5.3 V to 5 V with robust controller (lower right).

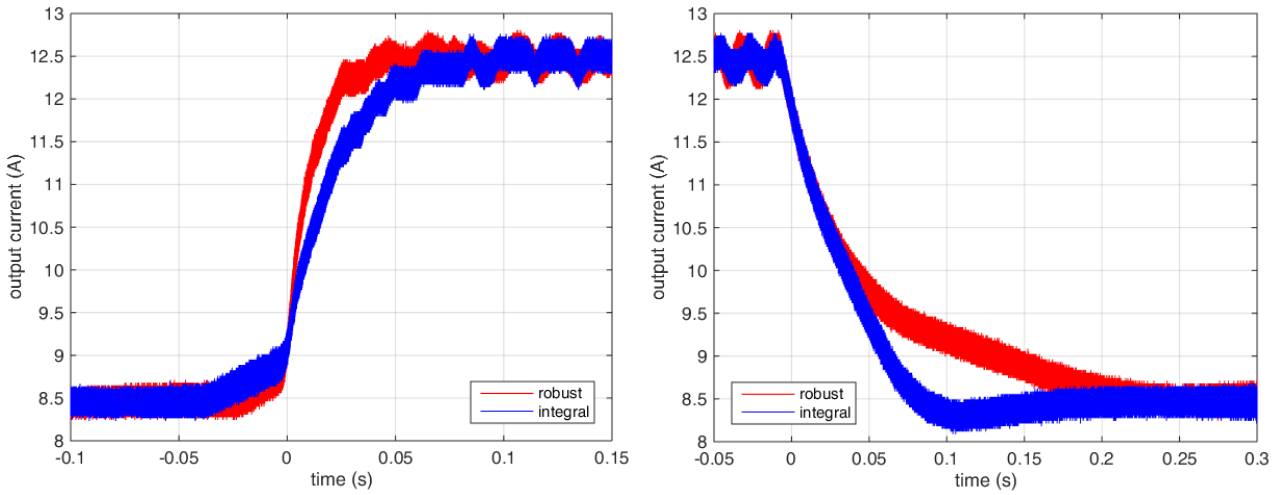

Fig. 19. Output current transient after set-point variation from 5 V to 5.3 V and vice versa: Integral controller (blue); robust controller (red).

As the figures show, the robust controller significantly improves the dynamic behavior in terms of transient duration compared with the integral controller, for both rising and falling transients. From a qualitative point of view, considering the falling transient, it can also be noticed that the response of the integral controller is overdamped, whereas that of the robust controller is underdamped, as exhibited in simulation. Instead, during the rising transient, both controllers exhibit an overdamped response, as it occurred in simulation.

Furthermore, it can be noticed that with both controllers it is possible to obtain such small variations of the output voltage that are required for obtaining much larger current variations from the electrolyzer.

5.3 Response to input voltage variation

In order to assess the system behavior in response to input voltage variation, a suitable Labview Virtual Instrument (VI) has been set up for programming the TDK-Lambda power supply using the RS232 interface. Therefore, it has been possible to apply step input voltage variations from 200 V to 180 V and vice versa. On the other hand, the reference output voltage has been kept constant at 5 V. The obtained input/output voltage and output current are shown in Fig. 20. As done before, for each transient direction, the acquired output current waveforms have been imported in Matlab and plotted superimposed on the same graph, as shown in Fig. 21.

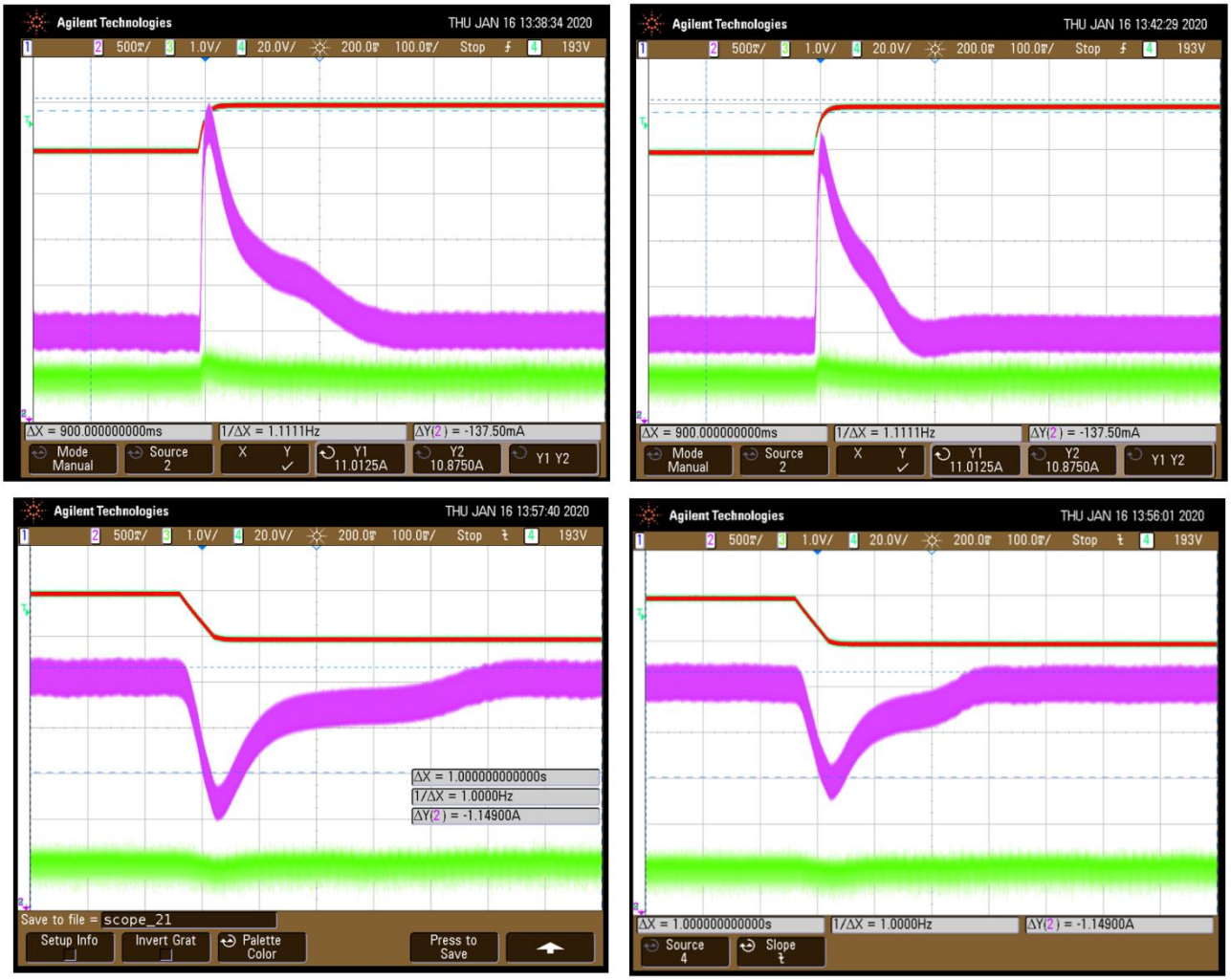

Fig. 20. Input voltage (dark red), output voltage (green) and output current (purple) transient after step input voltage variation: from 180 V to 200 V with integral controller (upper left); from 180 V to 200 V with robust controller (upper right); from 200 V to 180 V with integral controller (lower left); from 200 V to 180 V with robust controller (lower right).

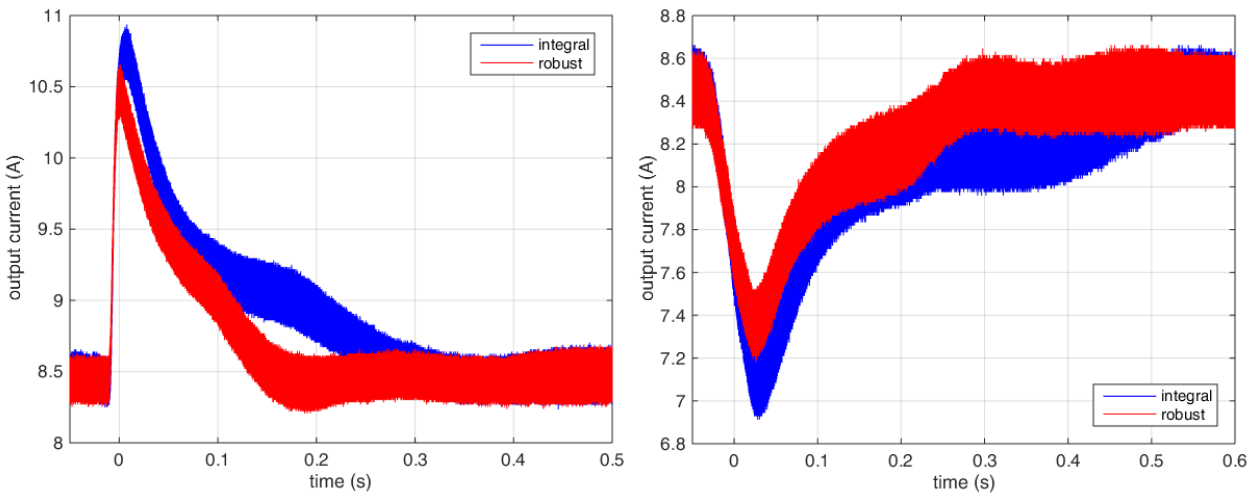

Fig. 21. Output current transient after input voltage variation from 200 V to 180 V and vice versa: integral controller (blue); robust controller (red).

As the figures show, using the robust controller the current peak after an input voltage variation is reduced compared with that obtained with the integral controller. Furthermore, a significant reduction of the transient duration can be noticed. The above considerations hold for both rising and falling transients.

It is worth noting that, although a step input voltage reference is applied using the Labview VI, the TDK-Lambda power supply, as all the real voltage sources, exhibits a non-null rising/falling time. For the chosen power supply, the rising/falling times are less than 20 ms and 100 ms, respectively. In any case, such values are much lower than those of any electromechanical conversion system.

6. CONCLUSIONS

In this work, a robust model-based controller has been designed for a buck-based, isolated, high-voltage-ratio DC/DC converter supplying a PEM electrolyzer from a μWECS. First, a more accurate dynamic model of the DC/DC converter-electrolyzer system has been devised that is particularly suitable for controller design. In fact, although the nonlinearities due to the set {full bridge converter, transformer, diode rectifier} are not included in the model, their effects are considered defining an equivalent turn ratio, which allows reproducing the real static characteristics of the converter. Thanks to this approach, a simple LTI model is obtained in which all the involved variables are DC-type. This model has been used to design a controller choosing a robust control methodology. This methodology allows defining a nominal model having few poles in a convenient location of the complex plane, and considering the remaining poles, with very low damping, as unmodelled dynamics. In this way, the remaining poles do not influence the structure of the controller, but only some controller parameters. Therefore, the second advantage is that the designed controller is robust against variations of the wind generator's voltage due to fluctuating wind speed. For this reason, not only the output of the converter (i.e., the input voltage of the electrolyzer) has a very low high-frequency ripple, but it also exhibits small overshoots and a reduced low-frequency content, extending the electrolyzer's lifespan. The validation performed on a circuit-oriented simulator (PLECS) confirmed the followed theoretical approach.

Besides the above-discussed advantages regarding the examined case study, this paper has the additional merit of showing a design approach that can be easily generalized to different case studies. In fact, model-based control has many advantages over other approaches at the disposal of the control engineer, like fuzzy or neural control. The first advantage is leveraging on the information contained in the mathematical model that is useful for control design. The second advantage is the opportunity of using well-developed control methodologies, which allow guaranteeing important properties among which robust stability, robust behavior, and optimal control. Finally, the steps for designing the controller are practically standardized; thus, the developing time of the controller is shorter.

The actual behavior of the designed robust controller has been compared to that of a classical integral controller by performing an experimental validation on a real test bench. The obtained results are coherent with those obtained in the simulations, showing faster transients and reduced over/undershoots in response to input voltage and output reference voltage variations.

REFERENCES

[1] E. Zoulias, E. Varkaraki, N. Lymberopoulos, C.N. Christodoulou, G.N. Karagiorgis, A review on water electrolysis, TCJST 4 (2) (2003) 41-71.

[2] N.L. Panwar, S.C. Kaushik, S. Kothari, Role of renewable energy sources in environmental protection: A review, Renewable and Sustainable Energy Reviews 15 (3) (2011) 1513-1524.

[3] Raul Sarrias-Mena, Luis M. Fernandez-Ramirez, Carlos Andres Garcia-Vazquez, Francisco Jurado, "Electrolyzer models for hydrogen production from wind energy systems." Int J Hydrogen Energy 2015; 40:2927-2938.

[4] Tao Zhou, Bruno Francois, "Modeling and control design of hydrogen production process for an active hydrogen/wind hybrid power system." Int J Hydrogen Energy 2009; 34:21-30.

[5] Mustafa Serdar Genc, Muhammet Celik, Ilyas Karasu, "A review on wind energy and wind–hydrogen production in Turkey: A case study of hydrogen production via electrolysis system supplied by wind energy conversion system in Central Anatolian Turkey." Renewable and Sustainable Energy Reviews 16 (2012) 6631–6646

[6] Pei-Hsing Huang, Jenn-Kun Kuo, Zong-Dain Wu, "Applying small wind turbines and a photovoltaic system to facilitate electrolysis hydrogen production." Int J Hydrogen Energy 2016; 41:8514-8524.

[7] K. Koiwa, A. Umemura, R. Takahashi and J. Tamura, "Stand-alone hydrogen production system composed of wind generators and electrolyzer," IECON 2013 - 39th Annual Conference of the IEEE Industrial Electronics Society, Vienna, 2013, pp. 1873-1879.

[8] A. M. O. Haruni, M. Negnevitsky, M. E. Haque and A. Gargoom, "A Novel Operation and Control Strategy for a Standalone Hybrid Renewable Power System," in IEEE Transactions on Sustainable Energy, vol. 4, no. 2, pp. 402-413, April 2013.

[9] C. N. Bhende, S. Mishra and S. G. Malla, "Permanent Magnet Synchronous Generator-Based Standalone Wind Energy Supply System," in IEEE Transactions on Sustainable Energy, vol. 2, no. 4, pp. 361-373, Oct. 2011.

[10] D. Guilbert, S. M. Collura, and A. Scipioni, "DC/DC converter topologies for electrolyzers: State-of-the-art and remaining key issues," International Journal of Hydrogen Energy, Vol. 42, 2017, 23966-23985.

[11] R. Samuel Rajesh Babu, Joseph Henry, "A Comparative Analysis of DC-DC Converters for Renewable Energy System," Proc. of Multi Conference of Engineers and Computer Scientists 2012, Vol. II, IMECS 2012, March 14-16, Hong Kong, 2012.

[12] A. Blinov, and A. Andrijanovits, "New DC/DC Converter for Electrolyser Interfacing with Stand-Alone Renewable Energy System," Electrical, Control and Communication Engineering, DOI: 10.2478/v10314-012-0004-1, 2012, pp. 24-29.

[13] D. S. Gautam, and A. K. S. Bhat, "A Comparison of Soft-Switched DC-to-DC Converters for electrolyzer Application," IEEE Trans. On Power Electronics, Vol. 28, No. 1, January 2013, pp. 54-63.

[14] S. M. Collura, D. Guilbert, A. Scipioni, G. Vitale, M. Luna, F. Alonge, and F. D'Ippolito, "Design and Experimental Validation of a High Voltage Ratio DC/DC Converter for Proton Exchange Membrane Electrolyzer Applications," International Journal of Hydrogen Energy, vol. 44, no. 14, pp. 7059-7072, 2019.

[15] I. Ngamroo, "Application of electrolyzer to alleviate power fluctuation in a stand-alone microgrid based on an optimal fuzzy PID control," *Electric Power and Energy Systems*, Elsevier, Vol. 43 (2012), pp. 969–976.

[16] D. Karaboga, and B. Basturk, "A powerful and efficient algorithm for numerical function optimization: artificial bee colony (ABC) algorithm," *Journal of Global Optimization* (2007), Vol. 39, pp. 459–471.

[17] R. M. Hilloowala, and A. M. Sharaf, "A rule-based fuzzy logic controller for a PWM inverter in a stand alone wind energy conversion scheme," *IEEE Trans. on Industry Applications*, Vol. 32, No. 1, January-February 1996, pp. 57-65.

[18] X. Li, Y. J. Song, S. B. Han, "Frequency control in micro-grid power system combined with electrolyzer system and fuzzy PI controller," *Journal of Power Sources*, Vol. 180, 2008, pp. 468–475.

[19] Ø. Ulleberg, "The importance of control strategies in PV–hydrogen systems," *Solar Energy*, Vol. 76, 2004, pp. 323–329.

[20] I. Ngamroo, "Robust coordinated control of electrolyzer and PSS for stabilization of microgrid based on PID-based mixed H_2/H_∞ control," *Renewable Energy*, Vol. 45, 2012, pp. 16-23.

[21] B. E. Muhando and R. W. Wies, "Nonlinear H_∞ Constrained Feedback Control for Grid-Interactive WECS Under High Stochasticity," in IEEE Transactions on Energy Conversion, vol. 26, no. 4, pp. 1000-1009, Dec. 2011.

[22] A. M. Howlader, N. Urasaki, A. Yona, T. Senjyu, and A. Y. Saber, "A new robust controller approach for a wind energy conversion system under high turbulence wind velocity," 2012 7th IEEE Conference on Industrial Electronics and Applications (ICIEA), Singapore, 2012, pp. 860-865.

[23] B. Qin et al., "Robust H_∞ Control of Doubly Fed Wind Generator Via State-Dependent Riccati Equation Technique," in IEEE Transactions on Power Systems, early access, 2018.

[24] A. Sferlazza, C. Albea-Sanchez, L. Martínez-Salamero, G. García and C. Alonso, "Min-Type Control Strategy of a DC–DC Synchronous Boost Converter," IEEE Trans. on Industrial Electronics, vol. 67, no. 4, pp. 3167-3179, April 2020.

[25] G. Vitale, M. Pucci, M. Luna, “Method and relevant system for converting mechanical energy from a generator actuated by a turbine into electric energy,” U.S. Patent 9856857, publication date: Jan. 2, 2018.

[26] M. Morari and E. Zafiriou, Robust Process Control. Englewood Cliffs, NJ: Prentice-Hall, 1989.

[27] F. Alonge, T. Cangemi, F. D’Ippolito “Identification and robust control of DC/DC converter Hammerstein model,” IEEE Transaction on Power Electronics, vol. 23, 2008, pp. 2990-3003.

[28] F. Alonge, R. Rabbeni, M. Pucci, and G. Vitale, "Identification and Robust Control of a Quadratic DC/DC Boost Converter by Hammerstein Model," IEEE Transactions on Industry Applications, Vol. 51, No. 5, September/October 2015, pp. 3975-3985.

[29] S. Skogestad and I. Postlethwait, Multivariable Feedback Control. Analysis and Design, John Wiley & Sons, 2001

[30] R.D. Middlebrook and S. Cuk, " A general unified approach to modelling switching-converter power stages," 1976 IEEE Power electronics specialists Conference.

[31] R. W. Erikson, and D. Maksimovic. "Fundamentals of power electronics: Kluwer academic." Norwell, USA (2001).

[32] M. H. Rashid, and H. M. Rashid, Spice for power electronics and electric power. CRC Press, 2005.